Experimental investigation of the stability of clinopyroxene in mid-ocean ridge basalts: The role of Cr and Ca/Al

Martin Voigt, Laurence A. Coogan, Anette von der Handt

2017

The final published version of this article can be found at:

https://doi.org/10.1016/j.lithos.2017.01.003

Experimental investigation of the stability of clinopyroxene in mid-ocean ridge basalts: the role of Cr and Ca/Al

Martin Voigt[a,b,1*], Laurence A. Coogan[a], Anette von der Handt[b,c]

[a] School of Earth and Ocean Sciences, University of Victoria, Victoria, BC V8W 3P6, Canada

[b] Institute of Earth and Environmental Sciences – Geochemistry, Albertstr. 23-B, 79104 Freiburg, Germany

[c] Department of Earth Sciences, University of Minnesota, 310 Pillsbury Drive SE, Minneapolis, MN 55455, USA

(*corresponding author: martin.voigt@get.obs-mip.fr)

Abstract

The change in the stability field of clinopyroxene in mid-ocean ridge basalt (MORB) as a function of pressure has been used widely as a geobarometer. Based on results from crystallization experiments using MORB-like compositions it has been suggested that MORB differentiation occurs at relatively high pressures at ultraslow- and slow-spreading ridges. However, differentiation requires the loss of substantial heat and it is unclear how this is possible at elevated pressures. To better understand the controls on the stability field of clinopyroxene in MORB-like compositions we

[1] Present address: GET – CNRS, 14 avenue Edouard Belin, 31400 Toulouse, France

report a series of experiments performed at 0.1 MPa in which the temperature of clinopyroxene saturation was determined in melts with variable Cr, Ca/Al and fO_2. The results show that increased Cr and Ca/Al lead to an expansion of the clinopyroxene stability field. Incorporating these results into a new model of MORB differentiation shows that realistic parental melt Cr contents can increase the temperature at which clinopyroxene saturation occurs relative to assuming a Cr-free melt (as is commonly the case). Likewise, high Ca/Al melts will saturate clinopyroxene earlier than low Ca/Al melts and their crystallization may provide an explanation for high Mg# clinopyroxene in oceanic gabbros. The newly calibrated geobarometer gives lower crystallization pressures for MORB at the slow-spreading SWIR than previous calibrations, but still suggests relatively higher pressures of crystallization with decreasing spreading rate.

Keywords

Mid-ocean ridge basalt; MORB; clinopyroxene; chromium; crystallization pressure; geobarometer

1. Introduction

The depth at which upward migrating melts begin to crystallize beneath mid-ocean ridges provides important constraints on the thermal structure of the lower crust and upper mantle at mid-ocean ridges; in turn this provides constraints on the dynamics of many ridge axis processes from mantle and melt flow patterns to hydrothermal fluid fluxes. The most commonly used approaches to determining the pressure of mid-ocean ridge basalt (MORB) crystallization revolve around the

changes in stability of clinopyroxene in MORB with increasing pressure. Based on comparison of the petrology and geochemistry of MORB, oceanic gabbros and the results of melting experiments conducted over a range of pressures it is widely suggested that MORB at slow-spreading ridges differentiate at moderate pressures (3-10 kbars) but those at fast-spreading ridges differentiate at low (≤3 kbars) pressure (e.g. Elthon, 1993; Grove et al., 1992; Herzberg, 2004; Villiger et al., 2007). This interpretation contrasts with thermal models that indicate that the release of the latent heat of crystallization of just small amounts of melt at high pressure will buffer the temperature of their surroundings (Sleep and Barth, 1997). Since most erupted MORB have crystallized a substantial fraction of their mass prior to eruption there appears to be an inconsistency between the petrological and modeling constraints on the thermal structure of slow-spreading ridges that needs resolving.

Experimental studies have demonstrated that the clinopyroxene phase field expands with increasing pressure in both simple (Presnall et al., 1978) and natural (Grove et al., 1992; Tormey et al., 1987; Yang et al., 1996) MORB-like compositions. This has led to numerous studies comparing the compositions of natural MORB with the compositions of melts predicted to be saturated with olivine, plagioclase and clinopyroxene at different pressures to investigate the pressure of MORB differentiation. It is important to note that this comparison is only valid for MORB that are co-saturated in olivine, plagioclase and clinopyroxene, and hence have crystallized a significant amount (and thus lost a significant amount of latent heat). Using this approach it has repeatedly been found that MORB from slow-spreading ridges commonly have compositions that are similar to the composition of olivine, plagioclase and clinopyroxene saturated melts equilibrated at relatively high pressures (3-10 kbars). In contrast, MORB from fast-spreading ridges generally have

69 compositions that are similar to the composition of olivine, plagioclase and
70 clinopyroxene saturated melts generated at low pressures (≤3 kbars; Grove et al.,
71 1992; Herzberg, 2004; Michael and Cornell, 1998; Tormey et al., 1987; Villiger et al.,
72 2007; Yang et al., 1996). Most of these approaches use some form of multi-
73 component projection scheme to account for the shifting of the phase boundaries in
74 composition space with difference in the abundance of other components (e.g. the
75 expansion of the olivine phase field with increased melt Na content; Grove et al.,
76 1992). A parallel line of reasoning has been used to conclude that some oceanic
77 gabbros crystallized at mantle pressures (3-10 kbars; Elthon, 1993; Elthon et al.,
78 1992). Expansion of the clinopyroxene stability field with increasing pressure means
79 that, all other things being equal, the first clinopyroxene to crystallize will have a
80 higher Mg# (molar ratio $Mg/(Mg+Fe^{2+})$, total Fe as Fe^{2+}) than that formed at lower
81 pressure because less olivine fractionation will occur prior to clinopyroxene
82 saturation. Based on the existence of clinopyroxene with Mg# > 0.88 in oceanic
83 gabbros, high pressure crystallization has been proposed (Elthon, 1993; Elthon et al.,
84 1992); however, high Mg# clinopyroxene also exist in oceanic gabbros from fast-
85 spreading ridges that formed at low pressure (Perk et al., 2007).

86 Alternative models to explain the "high-pressure differentiation" signatures in
87 MORB and oceanic gabbros have been proposed. These fall into two categories.
88 Firstly, there are models that invoke more complex magmatic processes in nature than
89 experiments. Perhaps the most important control is the crystallization process itself
90 where magma chambers that undergo cyclic replenishment and tapping and/or *in situ*
91 crystallization, can erupt magmas with compositions not controlled by the cotectics at
92 the crystallization pressure (Langmuir, 1989; O'Hara, 1977). For example, erupted
93 melts from a replenished and tapped magma chamber in which eruption follows

immediately after replenishment can produce lavas with very different Ca/Al than that of the olivine-plagioclase-clinopyroxene cotectic that the melts lay on prior to replenishment (Coogan and O'Hara, 2015; Nielsen, 1990). Secondly, there are models that call on alternative mechanisms to change the phase relations – it is this latter category that is the focus of this study. This study was designed to investigate changes in the stability field of clinopyroxene in MORB-like melts with changing: (i) melt Cr content, and (ii) melt CaO/Al_2O_3; fortuitously we also performed experiments at variable fO_2 and present these results, too.

Chromium is a highly compatible minor element in clinopyroxene meaning that increasing the concentration of the Cr-bearing clinopyroxene component in the melt will tend to stabilize clinopyroxene. This has been demonstrated experimentally in the system forsterite-anorthite-diopside in which the diopside field expands with increased Cr content (Onuma and Tohara, 1983). However the Cr content of the system in most experimental studies of MORB-like melts has not been considered. Indeed, most experimental studies that have been used to calibrate the role of pressure in clinopyroxene stabilization have been performed on relatively Cr-poor starting composition (or Cr concentrations have not been reported preventing evaluation of its effect). Likewise, most extant models of MORB differentiation do not include a Cr-bearing clinopyroxene component meaning changes in clinopyroxene stability with melt Cr content cannot be tested with these. The effect of Cr on the phase relations of MORB may be important because parental MORB are Cr-rich, generally having Cr-spinel as a liquidus or near-liquidus phase, and any regions of a crystal mush containing Cr-spinel will be buffered to high melt Cr-contents. This can also be seen in databases like PetDB (Lehnert et al., 2000), which shows a range of up to ~1000 ppm of Cr in MORB, and the highest frequency occurs at concentrations between 200

and 400 ppm Cr. The most primitive clinopyroxene in most oceanic gabbros contain >1 wt% Cr_2O_3 similar to mantle clinopyroxene. Additionally, since the Cr content of a Cr-spinel saturated basalt is strongly temperature dependent (Poustovetov and Roeder, 2001; Roeder and Reynolds, 1991), variations in mantle source temperature may lead to systematic variations in parental melt Cr content. This possibility makes understanding the role of Cr-spinel in MORB phase equilibria even more important.

Unlike the case just described for Cr, variations in melt CaO/Al_2O_3 are accounted for in most MORB-based geobarometers that compare the measured composition of a basalt with the location of the olivine-plagioclase-clinopyroxene phase boundary at different pressures *for that composition*. However, these are based on empirical projections of phase boundaries in composition space and are calibrated against existing experimental data on a limited range of starting compositions. Because changing the CaO/Al_2O_3 of a melt is intuitively expected to change the relative stability fields of plagioclase and clinopyroxene, and because the CaO/Al_2O_3 of MORB vary systematically (Klein and Langmuir, 1987), it is important that any change in phase equilibria with changing CaO/Al_2O_3 is accurately accounted for in these models. Further, the Mg# of the first clinopyroxene to precipitate from a MORB parental melt has been suggested to be as dependent on the parental melt CaO/Al_2O_3 as on the pressure of crystallization (Coogan et al., 2000). This can be directly tested by performing experiments specifically designed to vary just this compositional parameter.

Here we present the results of a low-pressure experimental study aimed at better understanding the stability of clinopyroxene during MORB differentiation. The primary goal of these experiments was to test the hypothesis that realistic variations in melt Cr contents in MORB are sufficient to noticeably change the stability of

clinopyroxene in MORB which we show is the case. A second goal of the experiments was to better calibrate the role of parental melt CaO/Al_2O_3 in controlling the stability of clinopyroxene in MORB. Finally, and fortuitously, due to an oxygen sensor problem in the furnace during some of the experiments we present results for some highly oxidized experiments. While these are far more oxidized than any natural MORB, these kinds of experiments are rarely performed (or at least reported) but provide useful information about the effect of changing oxygen fugacity. For example, effects of realistic fO_2 changes which are difficult to study experimentally due to their small magnitude, could be easier to resolve in our experiments. Combining the new experimental results with previously published results we develop a fractional crystallization model for MORB in which the effect of parental melt Cr content (as well as other compositional parameters) can be varied. We use this to demonstrate the small but significant effect of Cr on the temperature of clinopyroxene saturation in MORB and the pressures extracted from MORB geobarometers.

2. Experimental methods

2.1. Starting materials

All starting materials were synthesized using chemical grade, powdered SiO_2, TiO_2, Al_2O_3, Fe_2O_3, $Mg(OH)_2$, $CaCO_3$ and Na_2CO_3. The average of natural primitive MORB glass compositions reported by (Presnall and Hoover, 1987) was used as a base composition, but compositions with slightly different CaO/Al_2O_3 ratios were also synthesized (Table 1). Mixtures were homogenized with an agate mortar and pestle under methanol for ~20 min, subsequently devolatilized in a ceramic Al_2O_3 crucible at increasing temperatures of up to 900 °C for at least 12 h and homogenized again by

167 further grinding. Each mixture was fused in a platinum crucible at increasing
168 temperatures from 1250 to 1490 °C in air for 50 min, quenched in water, crushed in a
169 steel mortar and further ground and homogenized in an agate mortar and pestle under
170 methanol. Starting materials with the same major element composition but different
171 chromium contents were not separated until after these processes in order to prevent
172 undesired major element differences. Since preliminary experiments suggested that Cr
173 is rapidly lost to the atmosphere while fusing the starting materials in air, chromium
174 was added in sufficient quantities to induce precipitation of chromite, buffering the Cr
175 content in the melt. Chromium was added to relevant mixtures using a 1000 μg/g
176 chromium solution. The mixture was continuously homogenized with an agate mortar
177 and pestle during the evaporation of the solvent using a heat lamp, and subsequently
178 dried in a ceramic Al_2O_3 crucible at 150 °C for 12 h.

179 To accurately determine the starting composition, and its homogeneity, small
180 amounts of the powdered starting materials were fused for ca. 1.5 min at 1350 °C and
181 quenched in air in order to produce homogeneous glass for analysis (Table 1).
182 Compositional differences between individual glasses produced from the same
183 powder were determined to be within the limits of the 95% confidence interval of
184 analytical uncertainty in almost all cases. As expected, chromite crystals were
185 observed in the starting materials containing chromium. Mass balance calculations
186 using the amount of chromium added to the mixture suggest that less than 1 wt% of
187 chromite (assuming a molar Cr/Al ratio of 0.66) is present in these starting materials.

188 **2.2. Experimental setup**

189 The experiments can be divided into two sets, the first set comprising run
190 numbers #18 to #37, and run numbers from #57 onwards belong to the second set

191 (Table 2). The compositions of the starting materials are similar in these sets (C01a/d
192 and CaAl01a/c vs. C02a/b and CaAl02 in Table 1). However, the oxygen fugacity
193 (fO_2) in experiments of the first set was close to the quartz-fayalite-magnetite (QFM)
194 buffer, which is comparable to natural MORB melts (Cottrell and Kelley, 2011),
195 while fO_2 was ca. 3-5 orders of magnitude higher in the latter (cf. section "Oxygen
196 fugacity"). In the following text, the first experimental set will be referred to as "QFM
197 experiments", and the second set as "oxidized experiments".
198 All experiments were conducted at the School of Earth and Ocean Sciences,
199 University of Victoria, Canada using a purpose built one-atmosphere vertical tube gas
200 mixing furnace. Using methanol, an amount of (91±30) mg of the starting material
201 was attached to a loop of a 0.254 mm diameter platinum wire and subsequently
202 sintered using a blow torch and fused at 1350 °C for 30 min in air. The samples were
203 transferred into the furnace once it had equilibrated to the desired run conditions (T,
204 fO_2) and experiments were terminated by quenching in ambient air.
205 Sample temperature was measured with PtRh10-Pt and PtRh30-PtRh6
206 thermocouples located near the samples, which were calibrated against the gold
207 melting point of 1064.18 °C (ITS-90, 1990) with an uncertainty of ±2 °C. The
208 measured temperatures fluctuated within 4 °C on a time scale of < 10 s, likely due to
209 convection in the furnace, which may affect the accuracy of the absolute
210 temperatures. However, relative temperature differences between experiments
211 reported here are not affected by this effect because temperatures were averaged over
212 a longer time scale. Oxygen fugacity was controlled by a continuous flow of a CO_2-
213 CO gas mixture and measured using a SIRO2 C700+ solid electrolyte oxygen sensor,
214 showing fluctuations of ±0.3 in $\log(fO_2)$.

In order to reduce the loss of iron to the Pt wire (Grove, 1981), each wire was presaturated for 24 hr at the same conditions as the actual experimental run in a Deltech DT-31-V-OT vertical gas mixing furnace. After this presaturation run, the wires were cleaned and reused in the experiment. Loss of sodium to the furnace atmosphere was limited by reducing the gas flow rates to the lowest possible value (110-120 cm^3 min^{-1}) that allowed the fO_2 to be buffered in order to maximize the buildup of Na in the atmosphere around the sample.

2.3. Analytical methods

All starting materials and phases in experimental samples were analyzed with a 5-spectrometer CAMECA SX-100 electron microprobe at the University of Freiburg operating in the wavelength-dispersive mode, using a 15 keV accelerating voltage and a 20 nA beam current. Beam diameter was set to 5 μm for glass, feldspar, olivine and clinopyroxene analyses and focused for oxide minerals and Pt wires. On and off peak times of 20-40 s were used for major elements, and of up to 140 s for Cr using both LIF and PET crystals. Data reduction was done using the PAP-φ(ρZ) method (Pouchou and Pichoir, 1985). Data for all phases and elements except for Cr was normalized to USGS BHVO-2G (Wilson, 1997) with its composition taken from Jochum et al. (2005) based on averages of more than 50 analyses of this standard each week (Online Resource 1). For the average of 376 replicate analyses, determined correction factors are SiO_2: 0.985, TiO_2: 0.989, Al_2O_3: 0.994, FeO: 1.010, MgO: 0.963, CaO: 1.004, Na_2O: 0.991. For electron microprobe data, 1.96 standard errors of replicate analyses, corresponding to the interval where 95% of the values are expected to lie, are given and used for error propagation calculations.

Platinum wires were analyzed at the Department of Earth Sciences of the University of Minnesota using a JEOL JXA-8900R. Operating conditions were an accelerating voltage of 15 kV, beam current of 10 nA, a focused beam and on and off peak times of 40 s. Analyzed X-ray lines were Fe K_α and Pt M_α as well as Si K_α to monitor mixed analyses with the associated experimental glasses. Calibration standards were Fe metal, Pt metal and Si metal, respectively. The ZAF matrix correction method was applied.

3. Experimental results

3.1. Run products

Conditions of experimental runs as well as phases that were identified by optical miscroscopy and back-scattered electron (BSE) imaging in the polished cross sections of the samples in this study are listed in Table 2. Compositions of these phases are reported in Supplementary Table 1. Besides glass, all samples contain plagioclase and olivine. Therefore, no statement can be made about which of these two minerals is the liquidus phase for these compositions at atmospheric pressure. Clinopyroxene is present in the lowest temperature experiment for each starting material. For higher temperature experiments, it was only identified in samples with starting compositions that are spinel-saturated or exhibit a higher CaO/Al_2O_3 ratio (cf. Table 1). Abundant small chromite crystals are present in all samples with chromium-containing starting composition. Minor amounts of iron oxide minerals were found in some Cr-free run products.

3.2. Glass compositions

Since the glass phase in the run products represents the quenched melt, its

composition can be used to analyze the melt evolution as a function of temperature and bulk composition. The evolution of the melts in the QFM experiments and a 24 h run time is shown in Figure 1, showing that runs with chromite-saturated samples (C01d) contain less CaO compared to Cr-free runs at the same MgO contents. Comparing the glasses produced at different temperatures for the starting compositions with different Ca and Al content reveals that samples with a higher bulk Ca/Al ratio have similar glass CaO and Al_2O_3 contents at the lowest experimental temperature, but significantly more CaO and less Al_2O_3 at higher temperatures. Titanium, sodium and iron show a negative correlation with MgO, with iron showing some variability in absolute concentration when comparing different compositions. Similarly, silica concentrations increase with decreasing temperature and MgO, except for the lowest temperature experiment with the chromite-saturated composition, showing a decrease compared to the higher temperature experiment.

As was observed in the QFM experiments, in the oxidized experiments the calcium contents of the glass in the cpx-saturated samples containing chromium (C02b) are lower than in experimental runs with other compositions (Figure 2). Also, CaO in the glass in the CaAl02 starting composition (high Ca/Al bulk composition) at the highest temperature is higher compared to other starting compositions. Titanium and iron increase with decreasing MgO, however, the patterns show more variability compared to the QFM experiments. Furthermore, sodium and aluminum do not show steady trends as function of magnesium in samples of all compositions. Two other important differences to note are that cpx is found in samples of significantly higher absolute glass magnesium content despite the relatively similar starting composition. This is mainly caused by a higher fraction of cpx compared to olivine in the assemblage at oxidizing conditions. Also electron microprobe totals (calculated

assuming all Fe as FeO) of the glass analyses are consistently lower (<100 wt%), reflecting the higher Fe^{3+} content of the glasses.

3.3. Mineral compositions

Plagioclase anorthite contents show limited variation, from 0.72 to 0.80, across all the experiments. Iron contents in plagioclase of oxidized experiments are relatively high (up to 2.15 wt%) compared to QFM experiments, where iron contents are mostly below 1 wt%, consistent with previous studies in oxidized systems (e.g. Sugawara, 2001). There is also a compositional difference between olivines of the two experimental sets at different fO_2: $Mg\#_{ol}$ (molar ratio $Mg/(Mg+Fe^{2+})$ in olivine, total Fe as Fe^{2+}) are 0.85±0.03 in QFM experiments, and 0.93±0.03 in the oxidized set of experiments.

Clinopyroxene (cpx) is augite in all samples, and its major element composition does not differ significantly when comparing the experimental sets except for Mg#, which is higher in the first cpx to crystallize in experiments with a high Ca/Al bulk composition. As expected, cpx in samples with chromite-saturated starting composition show significantly higher amounts of Cr_2O_3, the maximum being 1.14(14) wt% (values in parentheses are uncertainty on the last digits) in sample C01d#20. Clinopyroxenes from QFM experiments contain higher Cr content than those from oxidized runs, which show a maximum of 0.45(9) wt% Cr_2O_3. However, no significant systematic difference in $^{Cr}_{Cpx\text{-}Liq}$ (defined as $^{Cr}_{Cpx}/\,^{Cr}_{Liq}$, where $^{Cr}_{i}$ is the molar cation fraction of Cr in phase i) is observed comparing these two sets of experiments. Chromium in cpx is below 0.10 wt% Cr_2O_3 in most experiments that were not doped with Cr, with the exception of sample C01a #18 where 0.41(4) wt% Cr_2O_3 was measured. This is still lower than in all chromite-saturated QFM

experiments; the most likely reason for this high Cr content is the exchange of chromium with a Cr-containing sample through the furnace atmosphere at high temperatures, facilitated by the small distance between the samples.

3.4. Oxygen fugacity

The systematic differences between glass and mineral compositions in the two sets of experiments, especially the higher iron contents in plagioclase and higher $Mg\#_{ol}$ and $Mg\#_{cpx}$ in the second set strongly suggests that fO_2 during these experiments was significantly above the QFM buffer, although fO_2 values calculated from oxygen sensor readings are close to QFM for these experiments. Since iron partitioning into Pt is dependent on fO_2 (Corrigan and Gibb, 1979; Donaldson, 1979), platinum wires from the relevant experiments were analyzed for their iron and platinum contents in order to calculate the true fO_2 value using equilibrium expressions for the liquid-metal Fe exchange by (Grove, 1981). The validity of this method of fO_2 estimation was tested using random samples from the first set of experiments, for which fO_2 measured by the oxygen sensor and values calculated from wire analyses show a reasonable agreement (Figure 3). The higher fO_2 values for the experiments with run numbers #57 onwards are also in agreement with estimations using the model of (Toplis, 2005) for the olivine-liquid Mg-Fe exchange equilibria, which is dependent on fO_2 (Figure 3). Thus, we use these high fO_2 experiments to investigate the role of fO_2 in controlling phase equilibria in MORB like compositions. An uncertainty of ± 1 in $\log(fO_2)$ was assigned to this parameter in further calculations for all experiments so that propagated uncertainties account for the variability shown by the different fO_2 estimates.

3.5. Loss of sodium and iron

Mass balance calculations were used to estimate the loss of sodium and iron from the samples during the experimental runs. Results indicate that up to 8.1(24) % (relative) of the sodium was lost in 24 h experiments, and up to 12.1(21) % (relative) was lost in 96 h runs. However, mass balance calculations indicate a gain of sodium for some samples of up to 13.6(39) % (relative), demonstrating that these values have to be treated with caution. A possible reason for this is the difficulty of analysis of sodium contents (e.g. caused by migration of Na under the electron beam, e.g. Spray and Rae, 1995) which might not be completely reflected in the standard deviations of analyses.

Loss of iron is up to 15.9 % (relative), but is not systematically higher in the longer running experiments. Experiment #34 (96 h) is an exception, with mass balance indicating a loss of 22 % (relative) FeO (Table 2). Estimates of iron loss are lower or even negative (i.e. suggesting Fe gain) for oxidized samples in most cases. This suggests that Fe may have been released from the Pt wires during experiments in which the pre-saturation was performed at more reducing conditions than the experimental conditions, which is consistent with the solubility of Fe in Pt (Corrigan and Gibb, 1979; Donaldson, 1979). Although iron oxides were identified in some samples, these minerals were not included into the mass balance calculations because it is not possible to distinguish between Fe-loss and abundance of iron oxides using mass balance. Therefore, the iron loss estimates should be regarded as maximum estimates, and must be partly caused by the presence of (metastable) iron oxides. Spinel was included in the mass balance calculations, adding uncertainties to the Fe-loss estimates because of the limited number and complexity of spinel analyses: The spinel compositions which were used for mass balance calculations are from averages

of multiple analyses with variation in iron content between 18% and 40% for QFM samples and 50% and 65% for oxidized samples.

3.6. Attainment of equilibrium

It is not possible to prove equilibrium in experiments such as those performed here. However, since inhomogeneities in minerals are inconsistent with thermodynamic equilibrium, phase homogeneity provides some insight into whether a close approach to equilibrium was attained. The vast majority of analyzed minerals in this study do not exhibit zoning or other inhomogeneities as verified through BSE investigations and which is reflected in the low standard errors calculated from analyses distributed through the mineral grains from core to rim. Individual plagioclase grains from the QFM experiments do show zoning of iron with higher Fe in the core compared to the rim. Since iron contents in plagioclase show a positive correlation with fO_2 (Sato, 1989; Sugawara, 2001), this zoning can be explained by initial growth of plagioclase under high oxygen fugacity due to the inevitable introduction of air into the furnace while the sample is being inserted and because the starting material was fused in air. However, this effect could only have been avoided by longer run times, which in turn lead to an increase in iron and sodium loss, and thus 24 h experiments were chosen as a compromise between homogeneity of phases and loss of components from the sample. Furthermore, $^{Fe^{2+}-Mg}_{Ol\text{-}Liq}$ (Table 2) are consistent with data from previous equilibrium studies, and the similarity of results obtained from 24 h and 48 h runs (see below) suggest that the samples represent a state close to equilibrium.

4. Discussion

The experiments in this study were designed to test for the effect of Cr (and Ca/Al ratios) of MORB melts on the relative temperature of saturation of clinopyroxene, compared to olivine and plagioclase, in MORB. The chosen temperature range from 1175 to 1217 °C produced samples with crystallinities ranging from 9.5% to 52.6%, and MgO contents of quenched melts lie between 7.17 wt% and 9.79 wt%. The general crystallization sequence of olivine and plagioclase at higher temperatures, followed by saturation of clinopyroxene at lower temperatures is consistent with previous experimental data with MORB compositions (e.g., Grove and Bryan, 1983; Sack et al., 1987; Yang et al., 1996). Comparing experiments of different starting composition, systematic and reproducible variations in the cpx saturation temperature can be observed (Figure 4).

4.1. The role of Cr in controlling clinopyroxene saturation in MORB

Clinopyroxene was found in Cr-containing samples at higher temperatures (1190 °C for C01d, 1205 °C for C02b) than in the equivalent Cr-free samples (1175 °C for C01a, 1198 °C for C02a). Furthermore, mass balance calculations (Table 2) suggest that a larger amount of cpx is present in chromite-saturated samples in comparison to the Cr-free bulk compositions in the respective runs at the lowest experimental temperature in each series. These results suggest that the very low abundance of Cr in the starting materials of most previous experiments will have led to later cpx saturation than in natural samples. This is consistent with abundant evidence that the first clinopyroxene to form grows from Cr-rich melts or in a reaction relationship with Cr-spinel. The absence of a Cr-bearing clinopyroxene component in most models used to simulate MORB differentiation (e.g. MELTs, Petrolog) neglects

404 the significant effect of Cr on the stability of cpx during MORB crystallization which
405 could lead further to systematic errors in the results of these models, most importantly
406 an underestimation of the cpx saturation temperature. The effect of chromium on the
407 stability of cpx can be explained by the high compatibility of this element in the
408 mineral as indicated by partition coefficients from ~ 3 to 36 (e.g., Duke, 1976; Hart
409 and Dunn, 1993; Skulski et al., 1994), which suggests that Cr stabilizes
410 clinopyroxene; i.e. the Cr-bearing component of clinopyroxene has a much lower
411 activity coefficient in pyroxene than melt.

412 **4.2. The role of Ca/Al in controlling clinopyroxene saturation in MORB**

413 In the experiments increasing the Ca/Al of the starting material results in
414 clinopyroxene saturation at a higher temperature (1190 °C for CaAl01c, 1205 °C for
415 CaAl02) (Figure 4). This is also reflected in mass balance calculations, indicating
416 larger amounts of cpx for higher Ca/Al ratio experiments (Table 2). The first cpx (i.e.
417 at the highest temperature) identified in experiments with a higher Ca/Al ratio show a
418 higher $Mg\#_{cpx}$ than the respective cpx in runs with lower bulk Ca/Al ratios in both
419 QFM runs (0.88(1) in high Ca/Al run CaAl01c #29 vs. 0.85(1) in lower Ca/Al runs
420 CaAl01a #26 and C01a #18) and oxidized experiments (0.84(2) in high Ca/Al run
421 CaAl02 #78 vs. 0.81(1) in C02a #63). This indicates that higher $Mg\#_{cpx}$ can be
422 crystallized from melts with higher Ca/Al ratios. Because the Ca/Al of a mantle melt
423 will change systematically with the extent of melting, if melts begin to crystallize
424 prior to being completely aggregated there is the potential for high Ca/Al melts to
425 crystallize within the MORB plumbing system. In this event some high Mg#
426 clinopyroxene are expected to form even if this crystallization occurs at low pressure.
427 This is consistent with observations of high Mg# clinopyroxene in oceanic gabbros

formed at the EPR (Perk et al., 2007) and questions previous interpretations that high Mg# clinopyroxene in oceanic gabbros from slow-spreading ridges record elevated pressure crystallization (Elthon, 1993; e.g. Elthon et al., 1992).

4.3. The effect of fO_2 on clinopyroxene saturation

Comparison of the results from the QFM experiments with those from the oxidized experiments reveals significant differences. In the oxidized experiments, clinopyroxene was found at higher temperatures, at 1198 °C in the Cr-free run (C02a) instead of 1175 °C (C01a, QFM run) and at 1205 °C with Cr-spinel saturated and higher Ca/Al starting compositions (C02b, CaAl02) compared to 1190 °C for the corresponding QFM experiments (Figure 4). However, experiments that were run under more oxidized conditions also exhibit a higher overall crystallinity compared to QFM experiments with similar bulk composition at the same temperature, making a direct comparison of clinopyroxene saturation timing as function of fO_2 difficult. Therefore, and due to the uncertainties associated with the determination of fO_2 (cf. section 'Oxygen fugacity'), further experiments are necessary to confirm these findings and improve our understanding of the role of the oxygen fugacity on MORB crystallization.

4.4. Effect of melt Cr content and Ca/Al on clinopyroxene geobarometers

MORB geobarometers are largely based on the temperature of cpx saturation, and numerous formulations exist (Danyushevsky et al., 1996; Grove et al., 1992; Herzberg, 2004; Michael and Cornell, 1998; Tormey et al., 1987; Villiger et al., 2007; Yang et al., 1996). The experimental glass compositions from this study were used as input for the clinopyroxene geobarometers of Herzberg (2004), Villiger et al. (2007) and Yang et al. (1996) to test how variations in Cr content and Ca/Al impact their

452 MORB geobarometers. In case of the geobarometer of Yang et al. (1996), the
453 correction factors for conversion of analytical data between the Smithsonian
454 Institution and MIT electron microprobes, published in the same paper, were applied
455 to our analytical data and this was found to give more consistent values. Results for
456 the experiments in which cpx was identified are presented in Figure 5. This figure
457 also shows results obtained with our extended and recalibrated version of the model
458 by Yang et al. (1996) which includes chromium, and which are discussed in the
459 'Modelling differentiation' section below.

460 Pressure estimates using the three published geobarometers for the chromite-
461 saturated samples are systematically higher compared to Cr-free samples with similar
462 bulk composition (Fig. 5). However, pressures calculated for samples with a higher
463 CaO/Al_2O_3 ratio of the starting composition are lower than, or similar to, the normal
464 Ca/Al samples in most cases. The magnitude of these differences varies among the
465 geobarometers. The largest pressure differences between the individual compositions
466 is predicted by the geobarometer of Villiger et al. (2007), and they are smaller for
467 geobarometers of Herzberg (2004) and Yang et al. (1996). The reason for the large
468 systematic variation in the Villiger et al. (2007) geobarometer are likely to be caused
469 by the calculation of pressures using only CaO and $Mg\#_{liq}$ in the melt as model
470 parameters. Since the parameterizations of Herzberg (2004) and Yang et al. (1996)
471 use a larger set of variables describing the melt composition, they are better able to
472 account for effects caused by variation of concentrations of these components.
473 Nevertheless, most of the geobarometers do not account for variability in the Cr
474 content of the system. The equations of Herzberg (2004) include Cr_2O_3 in the
475 empirically derived parameters for the projection which is used for the calculation of

476 pressures, however higher melt chromium contents lead to higher pressures estimates
477 in this geobarometer.

478 Although the experimental data show that a higher bulk CaO/Al_2O_3 ratio leads
479 to earlier saturation in cpx in terms of temperature and $Mg\#_{liq}$, this effect is partly
480 accounted for by available geobarometers. The fact that melt geobarometers mainly
481 give lower pressure estimates for samples of higher CaO/Al_2O_3 ratio suggests that the
482 phase equilibria are partially oversimplified in these models. As the melt CaO/Al_2O_3
483 in the calibration dataset of the Villiger et al. (2007) geobarometer are lower than the
484 highest values in our experiments, this is a potential reason for the observed pressure
485 differences, while the calibration ranges of the other two published geobarometers
486 include similar CaO/Al_2O_3 ratios. Additionally, absolute pressure estimates scatter
487 around the experimental pressure substantially. For example, for the QFM
488 experiments of this study the Villiger et al. (2007) barometer gives a range from +0.2
489 to -0.4 GPa and the Herzberg (2004) barometer a range from 0 to -0.3 GPa. This scale
490 of uncertainty clearly indicates that subtle variations in crystallization pressure (e.g.
491 Moho pressure versus base of the sheeted dikes) cannot be resolved with these
492 approaches.

493 ## 4.5. Modelling differentiation

494 To account for the effect of chromium, and a broader range of starting
495 material Ca/Al and range of fO_2 on clinopyroxene saturation, a fractional
496 crystallization model was constructed. The model of Yang et al. (1996), which in turn
497 is based on Grove et al. (1992), was used as a starting point because of the similar
498 scope and compositional range, the readily available sub-models from a common
499 source, and the use of equilibrium equations which can be easily inverted to predict

500 pressures. Apart from the cpx saturated samples in this study, the new formulation of
501 the model also includes other experimental data not included in the Yang calibration
502 and uses data from a total of 254 experiments (Table 3), with pressures ranging from
503 atmospheric pressure to 1 GPa. In the following, the principle and crystallization
504 scheme of the model is explained, followed by a detailed explanation of the new
505 model calibrations.

506 In the model of Yang et al. (1996) and its parent Grove et al. (1992) as well as
507 in the new model in this study, the crystallizing phases are determined by the location
508 of the melt phase relative to the predicted position of phase boundaries in composition
509 space. In the cpx-ol-plag pseudoternary projection of the cpx-ol-plag-quartz
510 pseudoquaternary, the olivine-plagioclase-melt (OPM) boundary is predicted as a line
511 perpendicular to the ol-plag sideline through the common position of the olivine-
512 plagioclase-augite-melt (OPAM) and olivine-plagioclase-augite-low-Ca-pyroxene-
513 melt (OPALM) points. The validity of this assumption can be verified by plotting the
514 predicted olivine/plagioclase ratio in the crystallizing assemblage versus the same
515 ratio calculated from the projection of the melt to the cpx-ol-plag pseudoternary.
516 Figure 6 shows that these two values show a good correlation for experiments
517 saturated in olivine and plagioclase. Depending on the side where the melt
518 composition is located, olivine or plagioclase is removed from the melt until the
519 boundary is reached and the respective other mineral (olivine or plagioclase) joins the
520 crystallizing assemblage. In contrast to the model of Yang et al. (1996), the projection
521 of the OPAM location is used here to predict the ratio of olivine to plagioclase during
522 olivine-plagioclase crystallization instead of the OPALM location. This has the
523 advantage of not requiring a new calibration of the OPALM location while working

524 equally well because both points overlap in the cpx-ol-plag projection (Grove et al.,
525 1992; Yang et al., 1996).

526 Olivine-plagioclase crystallization proceeds until augite saturation is reached.
527 This state is predicted by comparing the current predicted melt composition in the
528 crystallization model with modelled compositions of melts in equilibrium with augite,
529 olivine and plagioclase (see below) at each step. When the discrepancy between both
530 compositions reaches a minimum (i.e. when the discrepancy at the next crystallization
531 step would be larger than during the current step) augite joins the crystallizing
532 assemblage.

533 To account for the effect of oxygen fugacity on differentiation, all new or re-
534 calibrated equations (predicted OPAM compositions, plagioclase and augite
535 compositions (see below)) treat Fe^{2+} and Fe^{3+} individually. For the calibration of these
536 equations, Fe^{2+}/Fe^{3+} in the liquids is calculated from the empirical expression in
537 Kilinc et al. (1983) relating Fe^{2+}/Fe^{3+} in the liquid to the temperature, oxygen fugacity
538 and bulk composition. Partitioning of Fe into Fe^{2+} and Fe^{3+} in the application of the
539 model is calculated in the same way at each step in the model run.

540 Equations for prediction of OPAM compositions as well as for Fe^{3+} in
541 plagioclase and augite compositions were calibrated from the dataset in Table 3.
542 Where possible, analytical data from all studies was corrected to match data from the
543 Smithsonian Institution electron microprobe in order to account for interlaboratory
544 analytical differences. The calculation of the parameters in the calibrations were
545 performed using an effective variance technique (Orear, 1982) which is able to
546 account for uncertainties in all variables. By accounting for analytical uncertainties in
547 the calibration of the model, the effect of Cr that is seen in our experiments is
548 represented adequately in the model due to the high precision of our chromium

549 concentration data. The criterion of $p < 0.05$ was used to test for the significance of
550 parameters. In the new crystallization model constructed in this study, a step size of
551 1% of crystallization was used, since it was found that smaller step sizes do not affect
552 the results of the model runs. Temperatures were predicted at each step using the
553 equations of Ford et al. (1983).

554 **4.5.1. Prediction of augite-saturated melt (OPAM) compositions**

555 Modelling the composition of augite-saturated melts (OPAM) is a key element
556 in this crystallization model. It is used during olivine-plagioclase crystallization to
557 calculate the ratio of olivine to plagioclase crystallization, and the OPAM location
558 also determines the point of augite saturation (see above). The equations that are used
559 to model the position of melts saturated in augite, olivine and plagioclase (equivalent
560 to those given in Table 5 in Yang et al., 1996) were recalibrated in this study since the
561 equations of Yang et al. (1996) do not account for variations in chromium content or
562 oxygen fugacity and in order to incorporate the new experimental data reported here
563 (as well as new data compiled from the literature; Table 3). The new equations that
564 predict the composition of melts saturated in augite (Table 4) include melt chromium
565 content as well as Fe^{2+} and Fe^{3+} as separate variables. This does not change the
566 number of equations necessary, since the inclusion of two additional components is
567 balanced by fixing these as parameters in the equations. P-values for all newly
568 introduced parameters (Cr, Fe^{3+}) are below 0.05 and in most cases below 10^{-6},
569 reflecting the significance of these variables in modelling the composition of melts
570 multiply saturated in plagioclase, olivine and augite.

571 In comparison to the original calibration of Yang et al. (1996), most
572 coefficients in Table 4 are of similar magnitude. The largest difference can be seen in

573 the $^{liq}_{Ti}$ and $^{liq}_{Si} * {}^{liq}_{Ti}$ coefficients in the temperature equation, where both values are
574 significantly higher in Yang et al. (1996). This effect is largely caused by the
575 inclusion of experimental data in the CMAS+Ti system (Libourel, 1999) in this study.
576 Furthermore, values for coefficients X_{Fe} and X_{Si} in the temperature equation in Table
577 5 of Yang et al. (1996) have to be interchanged in order to yield reasonable
578 temperature predictions. Therefore, the change in algebraic sign compared to the new
579 calibration in Table 4 is only apparent.

580 The new equations for $^{liq}_{Al}$, $^{liq}_{Ca}$ and $^{liq}_{Mg}$ can be inverted and solved to yield
581 the pressure during crystallization, which is demonstrated for our experimental liquids
582 saturated with cpx in Figure 5. Comparison to the equivalent pressures calculated with
583 the original equations of Yang et al. (1996) indicates a significant improvement,
584 especially for the pressures estimated for the Cr-containing melts using $^{liq}_{Ca}$ and $^{liq}_{Al}$,
585 demonstrating the influence of chromium as a parameter in this type of model. The
586 errors remain largest for pressures obtained using $^{liq}_{Mg}$, as they are highly dependent
587 on analytical errors.

588 **4.5.2. Olivine crystallization and compositions**

589 Olivine is usually the first mineral to saturate in a cooling MORB parental
590 melt. In this model, the composition of olivine crystals are calculated as a solid
591 solution between pure forsterite and fayalite under the assumption of a Fe-Mg
592 distribution coefficient between melt and olivine of $^{Fe^{2+}\text{-}Mg}_{Ol\text{-}liq} = 0.30$, which was
593 adopted from Yang et al. (1996). The composition of olivine is recalculated in every
594 fractionation step.

595 **4.5.3. Plagioclase crystallization and compositions**

596 In the model, plagioclase is crystallizing from the melt either because the
597 initial melt composition lies on the plagioclase side of the OPM boundary, or after
598 olivine crystallization proceeded until the OPM boundary is reached. In the latter
599 case, the proportion of crystallizing olivine to plagioclase is calculated from the
600 relative position of the intersection of the OPM boundary with the olivine-plagioclase
601 sideline. The plagioclase composition is predicted using the expressions of Grove et
602 al. (1992), plus a new parameterization for the Fe^{3+} content. This parameterization
603 uses the equation

604 $$^{Plag}_{Fe^{3+}} = -0.055(10) + 0.061(10) * {}^{liq}_{Si} + 0.039(21) * {}^{liq}_{Al} + 0.055(11) * {}^{liq}_{Fe^{2+}}$$

605 $$+ 0.297(19) * {}^{liq}_{Fe^{3+}} + 0.122(21) * {}^{liq}_{Ca} + 0.070(12) * {}^{liq}_{Na}$$

606 $$+ 0.075(20) * {}^{liq}_{K}$$

607 which was calibrated using melt and plagioclase compositions from the dataset listed
608 in Table 3. In order to produce stoichiometric crystals, the amount of $^{Plag}_{Fe^{3+}}$ calculated
609 by the equation above is subtracted from the aluminum content calculated by the
610 expressions of Grove et al. (1992).

611 **4.5.4. Augite composition**

612 Augite compositions are predicted using empirically fitted expressions for the
613 eight stoichiometrically correct and linear independent cpx components $Mg_2Si_2O_6$
614 (enstatite), $Fe_2Si_2O_6$ (ferrosilite), $Ca_2Si_2O_6$ (wollastonite), $NaAlSi_2O_6$ (jadeite),
615 $NaCrSi_2O_6$ (ureyite), $CaAl_2SiO_6$ (Ca-Tschermak), $CaTiAl_2O_6$ (Ti-Tschermak) and
616 $Ca(Fe^{3+})_2SiO_6$ (Fe-Tschermak) (Table 5). The parameters in these equations were
617 derived from the dataset listed in Table 3. For this purpose, the Fe^{2+}/Fe^{3+} ratio was

618 estimated by first calculating the cation fractions based on 6 oxygens per formula
619 unit, and adjusting Fe^{2+} and Fe^{3+} in order to obtain 4 cations (permitting sufficient
620 Fe^{2+} is present). In a second step, the elemental composition is recast into the eight
621 cpx components plus SiO_2, which effectively sums all errors of the measured
622 compositions compared to a stoichiometrically perfect clinopyroxene into SiO_2. The
623 resulting component fractions are normalized to 100 %, and expressions for them as a
624 function of melt composition, temperature and pressure are obtained by regression
625 (Table 5).

626 **4.5.5. Application to experimental samples and validation of the model**

627 A comparison of the new fractional crystallization model with other existing
628 models (Ariskin et al., 1993; Ghiorso and Sack, 1995; Langmuir et al., 1992; Yang et
629 al., 1996) is shown in Figure 7 by running all calculations using the starting
630 composition C01a which is Cr-free and constraining fO_2 to the QFM buffer. In
631 addition, the model from this study was run using a bulk composition assuming 10
632 wt% iron loss, similar to the largest amount indicated by mass balance calculations
633 for experimental samples. Most models predict only small amounts of olivine or
634 plagioclase crystallization before the OPM boundary is reached, indicating that the
635 starting composition lies close to this boundary. Only the MELTS model (Ghiorso
636 and Sack, 1995) predicts a larger amount of plagioclase crystallization (6 wt%) before
637 the OPM boundary is reached. Predictions by the model of Yang et al. (1996) are
638 similar to the new model in this case, which is not surprising since fO_2 was
639 constrained to the QFM buffer, no chromium is present in the bulk composition, and
640 the basic principle of the model as well as a large part of the data sources for the
641 calibration are the same. The similarity of the differentiation up to the OPM boundary

642 also indicates that the use of the OPAM location for the prediction of this point
643 instead of the OPALM location as in Yang et al. (1996) does not have a significant
644 influence on the early differentiation estimation (cf. above). The model of Ariskin et
645 al. (1993) predicts significantly different FeO and Al_2O_3 contents during
646 crystallization. Fractional crystallization modelling in MELTS (Asimow and Ghiorso,
647 1998; Ghiorso and Sack, 1995) predicts substantially earlier crystallization of cpx, as
648 well as large discrepancies in concentrations of other components in comparison to
649 the experimental data. While the trend predicted by the model of Langmuir et al.
650 (1992) generally lies relatively close to the experimental data, significant deviations
651 exist in Al_2O_3 and SiO_2 concentrations. It should be noted that comparison of the
652 experimental and model compositions is not strictly valid, explaining differences
653 between the models and our experimental melt compositions: The aim of the
654 experiments is to equilibrate the same bulk composition at different temperatures,
655 more akin to equilibrium crystallization, while the models are all for fractional
656 crystallization.

657 The predicted anorthite content of plagioclase varies within ca. ±0.03 among
658 all models, with the trend of decreasing anorthite content with increasing
659 crystallization being of similar extent in all cases. The new model of this study
660 accounts for the incorporation of Fe in plagioclase, and the results of the experimental
661 runs (increasing Fe in plagioclase with progressing crystallization) are consistent with
662 the plagioclase composition predicted by the model. Predicted augite compositions
663 vary between the individual models, and some models do not predict sodium or
664 titanium concentrations. The new model is able to predict the experimental augite
665 composition relatively well and incorporates a Cr component, unlike most other

666 models, and predicts stoichiometrically correct clinopyroxene unlike some other
667 empirical models.

668 Therefore, the model developed in this study can be used to test the effect of
669 Cr on clinopyroxene saturation more accurately relative to other models. However,
670 crystallization of Cr-spinel is not included in the model, complicating the direct use of
671 the experimental starting compositions of this study as input for the model. Because
672 of this, an amount of 0.38 wt% Cr-spinel was mathematically removed from the
673 starting composition C01d (Cr-saturated) assuming a constant amount of Cr-spinel
674 during crystallization, and then used as a starting composition for the model. This
675 value of Cr-spinel abundance is obtained by the difference in chromium in the
676 analysed C01d starting material and chromium levels in experimental samples
677 (approx. 0.07 wt% Cr_2O_3). The composition of the Cr-spinel which was
678 mathematically removed from the C01d was averaged from electron microprobe
679 analyses of Cr-spinel in experimental samples (Cr_2O_3/Al_2O_3 =0.99, MgO/FeO^T=0.55).
680 A comparison of crystallization model runs at the QFM buffer with this starting
681 composition, and also with 0.14 wt% and 0.21 wt% Cr_2O_3 as well as one with the
682 same composition except for Cr, which was set to zero, is shown in Figure 8. This
683 clearly suggests that earlier saturation of augite is caused by higher chromium
684 contents in the melt, and demonstrates the potential effect of chromium on
685 clinopyroxene saturation and thus on results obtained from geobarometers based on
686 modelling cpx saturation. Figure 8 also shows that the onset of clinopyroxene
687 crystallization predicted by the model with Cr_2O_3 amounts of 0.07-0.14 wt% is
688 consistent with the experimental data. The first augites are predicted to contain 0.95
689 wt% of Cr_2O_3 in the 'chromite-saturated' model run with 0.07 wt% Cr_2O_3, which is

690 close to the upper end of chromium contents observed in early cpx in natural MORB
691 and oceanic gabbros (≤1.3 wt% Cr_2O_3 in general, e.g. Lehnert et al. (2000)).

692 **4.5.6. Application to natural samples**

693 In order to evaluate the effect of chromium on estimates of crystallization
694 pressures in MORB, $^{liq}_{Al}$, $^{liq}_{Ca}$ and $^{liq}_{Mg}$ equations derived in this study (Table 4) were
695 solved for pressure. Similarly to Villiger et al. (2007), the equation of $^{liq}_{Ca}$ was used
696 here which is least dependent on analytical errors, and applied to analyses of natural
697 glasses from mid-ocean ridge basalts obtained from the PetDB database (Lehnert et
698 al., 2000). Pressures were calculated iteratively by approximating $Fe^{2+}/\sum Fe$ ratios
699 according to Kilinc et al. (1983) and assuming conditions of the QFM buffer, using
700 temperatures estimated by the last equation in Table 4. Since these equations are only
701 applicable for liquids in equilibrium with cpx, the criterion of $Mg\#_{liq} < 0.6$ was
702 adopted from Villiger et al. (2007) in order to eliminate primitive, cpx undersaturated,
703 glasses from data sets. Although it is likely that cpx crystallized from most glasses
704 fulfilling this criterion, this cannot be verified and if melts are derived by 'complex'
705 magma chamber processes (e.g. including elements of magma mixing) then erupted
706 melts may not have all expected phases on their liquidus. Additionally, enriched
707 MORB were removed from the data set by excluding data with weight based
708 K_2O/TiO_2 ratios greater than 0.2. The number of data is further reduced by the limited
709 availability of analyses including chromium concentrations yielding a total of 746
710 data points.

711 The fast-spreading East Pacific Rise (EPR), the slow-spreading Mid Atlantic
712 Ridge (MAR) and the ultraslow-spreading South-West Indian Ridge (SWIR) were
713 selected to represent ridges of different spreading rates (e.g., Müller et al., 2008).

714 Pressures were also calculated for the data set of Jenner and O'Neill (2012), which
715 provides high precision Cr concentrations and has the added advantage of being
716 without interlaboratory biases. Only compositions marked as 'spreading ridge' were
717 used, and the same criteria for eliminating primitive glasses and hot spot affected
718 compositions as for the PetDB samples were applied for this data set. Furthermore,
719 this data set was subdivided into intermediate- to fast-spreading ridges and slow-
720 spreading ridges (full spreading rates less than 55 mm/year) based on data of Müller
721 et al. (2008). For comparison, pressures were also calculated with the same technique
722 but with the assumption of chromium free samples, and using the geobarometers of
723 Villiger et al. (2007) and Herzberg (2004).

724 The results (Figures 9 and 10) suggest that inclusion of chromium into our
725 melt-composition based geobarometer significantly affects the pressure estimates. The
726 mean of the pressure distributions for the EPR calculated with the new model from
727 this study is 0.27 GPa, whereas a value of 0.35 GPa is obtained when ignoring
728 chromium contents. The corresponding values for the MAR are 0.38 GPa vs. 0.48
729 GPa and 0.40 GPa vs. 0.55 GPa for the SWIR. For intermediate- to fast-spreading
730 ridges in the data set of Jenner and O'Neill (2012), the corresponding values are 0.20
731 GPa vs. 0.27 GPa, and 0.33 GPa vs 0.42 GPa for slow-spreading ridges. With a
732 difference of 0.15 GPa, the magnitude of the effect of Cr is largest for the ultraslow-
733 spreading SWIR, but systematically lower pressures are also derived for the EPR and
734 MAR when incorporating measured Cr contents into the calculations. The same
735 systematic difference can be seen between pressures calculated using the data set of
736 Jenner and O'Neill (2012): The difference of 0.09 GPa, which is obtained when
737 including Cr into the geobarometer for slow-spreading ridge data, is larger compared
738 to the corresponding value for data of faster-spreading ridges (0.07 GPa). However,

739 these differences in magnitude arise from the higher mean in reported chromium
740 contents from the slower-spreading ridges, which suggests that the sampled rocks
741 were subject to a lower amount of differentiation (consistent with the well-known
742 higher average Mg# of MORB from slow-spreading ridges (e.g., Niu and Batiza,
743 1993)).

744 Comparison of absolute pressure estimates of the new model to values
745 obtained from the equations of Villiger et al. (2007) and Herzberg (2004) (Figures 9
746 and 10) show that the new calibration including melt Cr content gives similar depths
747 of crystallization to these previous approaches for all but the slowest spreading ridges
748 (means of 0.29 GPa and 0.28 GPa for the EPR and equations of Villiger et al. (2007)
749 and Herzberg (2004), respectively, and means of 0.48 GPa and 0.33 GPa for the MAR
750 and the same equations). This suggests that pressure estimates resulting from these
751 two existing geobarometers are not affected significantly by chromium for these
752 MOR settings. In contrast, our new model predicts systematically lower pressures for
753 samples from the ultraslow-spreading SWIR, especially compared to Villiger et al.
754 (2007) (a mean of 0.63 GPa result from application of the equations of Villiger et al.
755 (2007), and 0.50 GPa using equations in Herzberg (2004)). The distribution of
756 pressures calculated for the data set of Jenner and O'Neill (2012) using the method of
757 Villiger et al. (2007) shows a significant number of pressures below zero, which is
758 likely the result of interlaboratory analytical differences between the MORB data set
759 and the data used to calibrate the geobarometer or calibration problems in this
760 geobarometer.

761 Wanless and Shaw (2012) calculated crystallization pressures for MORB from
762 the fast-spreading EPR and the intermediate-spreading Juan de Fuca Ridge (JdFR)
763 based on the volatile composition of melt inclusions. Their results suggest an inverse

764 correlation between spreading rate and crystallization depth, which is similar to the
765 results seen in Figures 9 and 10. However, the absolute median crystallization
766 pressures calculated using their method (~ 0.05 GPa for the EPR and ~ 0.09 GPa for
767 the JdFR) are smaller than pressures estimated from our equation and those of Villiger
768 et al. (2007) and Herzberg (2004). These differences could partly result from different
769 sampling biases in the used data sets, which cannot be tested in detail as Cr contents
770 of the host rocks analysed by Wanless and Shaw (2012) are unknown.

771 **4.5.7. Quantifying the influence of Cr on clinopyroxene barometers**

772 The new crystallization model developed in this study (see above) allows us to
773 test the influence of chromium on the predicted crystallization pressures. In order to
774 illustrate the magnitude of this effect, pressures were calculated using the $^{liq}_{Ca}$
775 equation in Table 4 and the same iterative technique described above. The mean of all
776 glasses from Jenner and O'Neill (2012) after elimination of primitive and enriched
777 samples was used as base composition, and chromium was varied. Figure 11 shows
778 the effect of variation in chromium content on predicted crystallization pressures,
779 suggesting that melt chromium contents at clinopyroxene saturation has a significant
780 effect on the pressure estimates and should be included in barometric calculations to
781 obtain accurate results.

782 ## 4.6. Conclusions

783 A series of low pressure experiments designed to evaluate the roles of Cr and
784 Ca/Al in controlling the stability of clinopyroxene in MORB-like melt compositions
785 demonstrate the following: (i) realistic parental melt Cr contents will lead to
786 variations in, and generally expand, the clinopyroxene stability field relative to that
787 determined in most previous studies; (ii) melts with higher Ca/Al will, all other things

788 being equal, crystallize clinopyroxene earlier (i.e. at higher temparture) than melts
789 with lower Ca/Al. Crystallization of high Ca/Al parental melts is a plausible
790 explanation of high $Mg\#_{cpx}$ in oceanic gabbros; (iii) incorporation of the new
791 experimental data into a model of MORB differentiation shows potentially non-trivial
792 differences in the timing of clinopyroxene saturation and calculated crystallization
793 pressures occur when Cr is taken into account. Application to natural MORB
794 compositions suggests that the difference of pressure estimates from our new
795 geobarometer to those from previous geobarometers is largest for slow-spreading
796 ridges such as the SWIR, but negligible for the fast-spreading EPR.

797 We note that while we have demonstrated that the Cr-content of a melt must
798 be considered when evaluating the conditions under which clinopyroxene will
799 crystallize, further work is required to fully quantify this. First, Cr is known to
800 dissolve in a melt as both Cr^{2+} and Cr^{3+}, and likely has at least one more complex
801 component. Hence the activity of the Cr-bearing clinopyroxene component in the melt
802 is likely to be a complex function of melt composition, temperature and fO_2 (Berry et
803 al., 2006; Colson et al., 2000; Hanson and Jones, 1998). Additionally, we do not know
804 what the Cr-bearing component in natural clinopyroxene crystallizing from MORB is
805 and our assumption of ureyite, and of the parameterization developed for this (Table
806 5), should be further tested. Extending the experiments on the effect of chromium on
807 geobarometers to higher pressures would help improve our understanding of the
808 influence of chromium on MORB crystallization at mid-ocean ridges. While we have
809 investigated the roles of melt Cr and Ca/Al in controlling the stability field of
810 clinopyroxene we note that other factors (e.g. mixing processes, *in situ* crystallization)
811 likely influence clinopyroxene saturation in MORB and oceanic gabbros as well.
812 However, we showed that the incorporation of Cr can produce small but significant

effects in the parametrization of geobarometers, which may further resolve discrepancies between experimental data, thermodynamic considerations and natural observations.

Acknowledgements

We would like to thank Philipp Brandl and an anonymous reviewer for thoughtful comments that helped us improve the manuscript. Hiltrud Müller-Sigmund and Paul Robert Keppner for their assistance during electron microprobe measurements and sample preparation, respectively. MV was funded by a DAAD scholarship during his stay at the University of Victoria. Experiments were funded through an NSERC grant to LAC.

References

Ariskin, A.A., Frenkel, M.Y., Barmina, G.S., Nielsen, R.L., 1993. COMAGMAT: a Fortran program to model magma differentiation processes. Comput. Geosci. 19, 1155–1170. doi:10.1016/0098-3004(93)90020-6

Asimow, P.D., Ghiorso, M.S., 1998. Algorithmic modifications extending MELTS to calculate subsolidus phase relations. Am. Mineral. 83, 1127–1132.

Baker, D.R., Eggler, D.H., 1987. Compositions of anhydrous and hydrous melts coexisting with plagioclase, augite, and olivine or low-Ca pyroxene from 1 atm to 8 kbar; application to the Aleutian volcanic center of Atka. Am. Mineral. 72, 12–28.

833 Berry, A.J., O'Neill, H.S.C., Scott, D.R., Foran, G.J., Shelley, J.M.G., 2006. The
834 effect of composition on Cr^{2+}/Cr^{3+} in silicate melts. Am. Mineral. 91, 1901–
835 1908.
836 Colson, R.O., Colson, M.C., Nermoe, M.K.B., Floden, A.M., Hendrickson, T.R.,
837 2000. Effects of aluminum on Cr dimerization in silicate melts and
838 implications for Cr partitioning and redox equilibria. Geochim. Cosmochim.
839 Acta 64, 527–543. doi:10.1016/S0016-7037(99)00202-1
840 Coogan, L.A., Kempton, P.D., Saunders, A.D., Norry, M.J., 2000. Melt aggregation
841 within the crust beneath the Mid-Atlantic Ridge: evidence from plagioclase
842 and clinopyroxene major and trace element compositions. Earth Planet. Sci.
843 Lett. 176, 245–257. doi:10.1016/S0012-821X(00)00006-6
844 Coogan, L.A., O'Hara, M.J., 2015. MORB differentiation: In situ crystallization in
845 replenished-tapped magma chambers. Geochim. Cosmochim. Acta 158, 147–
846 161.
847 Corrigan, G., Gibb, F.G.F., 1979. The loss of Fe and Na from a basaltic melt during
848 experiments using the wire-loop method. Mineral. Mag. 43, 121–126.
849 doi:10.1180/minmag.1979.043.325.10
850 Cottrell, E., Kelley, K.A., 2011. The oxidation state of Fe in MORB glasses and the
851 oxygen fugacity of the upper mantle. Earth Planet. Sci. Lett. 305, 270–282.
852 doi:10.1016/j.epsl.2011.03.014
853 Danyushevsky, L.V., Sobolevz, A.V., Dmitrievz, L.V., 1996. Estimation of the
854 pressure of crystallization and H_2O content of MORB and BABB glasses:
855 calibration of an empirical technique. Mineral. Petrol. 57, 185–204.
856 doi:10.1007/BF01162358

857 Donaldson, C.H., 1979. Composition changes in a basalt melt contained in a wire
858 loop of Pt_{80} Rh_{20}: effects of temperature, time, and oxygen fugacity. Mineral.
859 Mag. 43, 115–119. doi:10.1180/minmag.1979.043.325.09
860 Duke, J.M., 1976. Distribution of the Period Four Transition Elements among
861 Olivine, Calcic Clinopyroxene and Mafic Silicate Liquid: Experimental
862 Results. J. Petrol. 17, 499–521. doi:10.1093/petrology/17.4.499
863 Elthon, D., 1993. The crystallization of mid-ocean ridge basalts at moderate and high
864 pressures. Eur. J. Mineral. 5, 1025–1037.
865 Elthon, D., Stewart, M., Ross, D.K., 1992. Compositional trends of minerals in
866 oceanic cumulates. J. Geophys. Res. 97, 15189–15199.
867 doi:10.1029/92JB01187
868 Ford, C.E., Russell, D.G., Craven, J.A., Fisk, M.R., 1983. Olivine-liquid equilibria:
869 temperature, pressure and composition dependence of the crystal/liquid cation
870 partition coefficients for Mg, Fe^{2+}, Ca and Mn. J. Petrol. 24, 256–266.
871 doi:10.1093/petrology/24.3.256
872 Ghiorso, M.S., Sack, R.O., 1995. Chemical mass transfer in magmatic processes IV.
873 A revised and internally consistent thermodynamic model for the interpolation
874 and extrapolation of liquid-solid equilibria in magmatic systems at elevated
875 temperatures and pressures. Contrib. Mineral. Petrol. 119, 197–212.
876 doi:10.1007/BF00307281
877 Grove, T.L., 1981. Use of FePt alloys to eliminate the iron loss problem in 1
878 atmosphere gas mixing experiments: theoretical and practical considerations.
879 Contrib. Mineral. Petrol. 78, 298–304. doi:10.1007/BF00398924

880 Grove, T.L., Bryan, W.B., 1983. Fractionation of pyroxene-phyric MORB at low
881 pressure: an experimental study. Contrib. Mineral. Petrol. 84, 293–309.
882 doi:10.1007/BF01160283
883 Grove, T.L., Kinzler, R.J., Bryan, W.B., 1992. Fractionation of Mid-Ocean Ridge
884 Basalt (MORB), in: Phipps Morgan, J., Blackman, D.K., Sinton, J.M. (Eds.),
885 Mantle Flow and Melt Generation at Mid-Ocean Ridges. American
886 Geophysical Union, pp. 281–311.
887 Grove, T.L., Kinzler, R.J., Bryan, W.B., 1990. Natural and experimental phase
888 relations of lavas from Serocki volcano, in: Detrick, R., Honnorez, J., Bryan,
889 W.B., Juteau, T. (Eds.), Proceedings of the Ocean Drilling Program, Scientific
890 Results. pp. 9–17. doi:10.2973/odp.proc.sr.106109.114.1990
891 Hanson, B., Jones, J.H., 1998. The systematics of Cr^{3+} and Cr^{2+} partitioning between
892 olivine and liquid in the presence of spinel. Am. Mineral. 83, 669.
893 Hart, S.R., Dunn, T., 1993. Experimental cpx/melt partitioning of 24 trace elements.
894 Contrib. Mineral. Petrol. 113, 1–8. doi:10.1007/BF00320827
895 Herzberg, C., 2004. Partial crystallization of mid-ocean ridge basalts in the crust and
896 mantle. J. Petrol. 45, 2389–2405. doi:10.1093/petrology/egh040
897 Jenner, F.E., O'Neill, H.S.C., 2012. Analysis of 60 elements in 616 ocean floor
898 basaltic glasses. Geochem. Geophys. Geosystems 13.
899 doi:10.1029/2011GC004009
900 Juster, T.C., Grove, T.L., Perfit, M.R., 1989. Experimental constraints on the
901 generation of FeTi basalts, andesites, and rhyodacites at the Galapagos
902 Spreading Center, 85 W and 95 W. J. Geophys. Res. 94, 9251–9274.
903 doi:10.1029/JB094iB07p09251

904 Kilinc, A., Carmichael, I.S.E., Rivers, M.L., Sack, R.O., 1983. The ferric-ferrous ratio
905 of natural silicate liquids equilibrated in air. Contrib. Mineral. Petrol. 83, 136–
906 140. doi:10.1007/BF00373086
907 Klein, E.M., Langmuir, C.H., 1987. Global correlations of ocean ridge basalt
908 chemistry with axial depth and crustal thickness. J. Geophys. Res. 92, 8089–
909 8115. doi:10.1029/JB092iB08p08089
910 Langmuir, C., Klein, E., Plank, T., 1992. Petrological systematics of mid-ocean ridge
911 basalts: Constraints on melt generation beneath ocean ridges, in: Morgan, J.,
912 Blackman, D., Sinton, J. (Eds.), Mantle Flow and Melt Generation at Mid-
913 Ocean Ridges. American Geophysical Union, pp. 183–183.
914 Langmuir, C.H., 1989. Geochemical consequences of in situ crystallization. Nature
915 340, 199–205.
916 Lehnert, K., Su, Y., Langmuir, C.H., Sarbas, B., Nohl, U., 2000. A global
917 geochemical database structure for rocks. Geochem. Geophys. Geosystems 1.
918 doi:10.1029/1999GC000026
919 Libourel, G., 1999. Systematics of calcium partitioning between olivine and silicate
920 melt: implications for melt structure and calcium content of magmatic
921 olivines. Contrib. Mineral. Petrol. 136, 63–80. doi:10.1007/s004100050524
922 Libourel, G., Boivin, P., Biggar, G.M., 1989. The univariant curve liquid = forsterite
923 + anorthite + diopside in the system CMAS at 1 bar: solid solutions and melt
924 structure. Contrib. Mineral. Petrol. 102, 406–421. doi:10.1007/BF00371084
925 Michael, P.J., Cornell, W.C., 1998. Influence of spreading rate and magma supply on
926 crystallization and assimilation beneath mid-ocean ridges: Evidence from
927 chlorine and major element chemistry of mid-ocean ridge basalts. J. Geophys.
928 Res. 103, 18325–18356. doi:10.1029/98JB00791

929 Müller, R.D., Sdrolias, M., Gaina, C., Roest, W.R., 2008. Age, spreading rates, and
930 spreading asymmetry of the world's ocean crust. Geochem. Geophys.
931 Geosystems 9. doi:10.1029/2007GC001743
932 Nielsen, R.L., 1990. Simulation of igneous differentiation processes. Rev. Mineral.
933 Geochem. 24, 65–105.
934 Niu, Y., Batiza, R., 1993. Chemical variation trends at fast and slow spreading mid-
935 ocean ridges. J. Geophys. Res. Solid Earth 98, 7887–7902.
936 doi:10.1029/93JB00149
937 O'Hara, M.J., 1977. Geochemical evolution during fractional crystallisation of a
938 periodically refilled magma chamber. Nature 266, 503–507.
939 Onuma, K., Tohara, T., 1983. Effect of chromium on phase relations in the join
940 forsterite-anorthite-diopside in air at 1 atm. Contrib. Mineral. Petrol. 84, 174–
941 181. doi:10.1007/BF00371283
942 Orear, J., 1982. Least squares when both variables have uncertainties. Am. J. Phys.
943 50, 912. doi:10.1119/1.12972
944 Perk, N.W., Coogan, L.A., Karson, J.A., Klein, E.M., Hanna, H.D., 2007. Petrology
945 and geochemistry of primitive lower oceanic crust from Pito Deep:
946 implications for the accretion of the lower crust at the Southern East Pacific
947 Rise. Contrib. Mineral. Petrol. 154, 575–590. doi:10.1007/s00410-007-0210-z
948 Pouchou, J.L., Pichoir, F., 1985. PAP φ(ρZ) procedure for improved quantitative
949 microanalysis. Microbeam Anal. 104–106.
950 Poustovetov, A., Roeder, P., 2001. Numerical modeling of major element distribution
951 between chromian spinel and basaltic melt, with application to chromian
952 spinel in MORBs. Contrib. Mineral. Petrol. 142, 58–71.
953 doi:10.1007/s004100100272

954 Presnall, D.C., Dixon, S.A., Dixon, J.R., O'Donnell, T.H., Brenner, N.L., Schrock,
955 R.L., Dycus, D.W., 1978. Liquidus phase relations on the join diopside-
956 forsterite-anorthite from 1 atm to 20 kbar: their bearing on the generation and
957 crystallization of basaltic magma. Contrib. Mineral. Petrol. 66, 203–220.
958 doi:10.1007/BF00372159
959 Presnall, D.C., Hoover, J.D., 1987. High pressure phase equilibrium constraints on the
960 origin of mid-ocean ridge basalts, in: Mysen, B.O. (Ed.), Magmatic Processes:
961 Physicochemical Principles. The Geochemical Society, pp. 75–89.
962 Reynolds, J.R., Langmuir, C.H., 1997. Petrological systematics of the Mid-Atlantic
963 Ridge south of Kane: Implications for ocean crust formation. J. Geophys. Res.
964 102, 14915–14. doi:10.1029/97JB00391
965 Roeder, P.L., Reynolds, I., 1991. Crystallization of chromite and chromium solubility
966 in basaltic melts. J. Petrol. 32, 909–934. doi:10.1093/petrology/32.5.909
967 Sack, R.O., Walker, D., Carmichael, I.S., 1987. Experimental petrology of alkalic
968 lavas: constraints on cotectics of multiple saturation in natural basic liquids.
969 Contrib. Mineral. Petrol. 96, 1–23. doi:10.1007/BF00375521
970 Sano, T., Fujii, T., Deshmukh, S.S., Fukuoka, T., Aramaki, S., 2001. Differentiation
971 processes of Deccan Trap basalts: contribution from geochemistry and
972 experimental petrology. J. Petrol. 42, 2175–2195.
973 doi:10.1093/petrology/42.12.2175
974 Sato, H., 1989. Mg-Fe partitioning between plagioclase and liquid in basalts of Hole
975 504B, ODP Leg 111: a study of melting at 1 atm, in: Becker, K., Sakai, H.
976 (Eds.), Proceedings of the Ocean Drilling Program, Scientific Results. p. 17—
977 26. doi:doi:10.2973/odp.proc.sr.111.113.1989

978 Scoates, J.S., Cascio, M.L., Weis, D., Lindsley, D.H., 2006. Experimental constraints
979 on the origin and evolution of mildly alkalic basalts from the Kerguelen
980 Archipelago, Southeast Indian Ocean. Contrib. Mineral. Petrol. 151, 582–599.
981 doi:10.1007/s00410-006-0070-y
982 Shi, P., 1993. Low-Pressure Phase Relationships in the System Na_2O—CaO—FeO—
983 MgO—Al_2O_3—SiO_2 at 1100°C, with Implications for the Differentiation of
984 Basaltic Magmas. J. Petrol. 34, 743–762. doi:10.1093/petrology/34.4.743
985 Shi, P., Libourel, G., 1991. The effects of FeO on the system CMAS at low pressure
986 and implications for basalt crystallization processes. Contrib. Mineral. Petrol.
987 108, 129–145. doi:10.1007/BF00307332
988 Skulski, T., Minarik, W., Watson, E.B., 1994. High-pressure experimental trace-
989 element partitioning between clinopyroxene and basaltic melts. Chem. Geol.
990 117, 127–147. doi:10.1016/0009-2541(94)90125-2
991 Sleep, N.H., Barth, G.A., 1997. The nature of oceanic lower crust and shallow mantle
992 emplaced at low spreading rates. Tectonophysics 279, 181–191.
993 doi:10.1016/S0040-1951(97)00121-2
994 Spray, J.G., Rae, D.A., 1995. Quantitative electron-microprobe analysis of alkali
995 silicate glasses: A review and user guide. Can. Mineral. 33, 323–323.
996 Sugawara, T., 2001. Ferric iron partitioning between plagioclase and silicate liquid:
997 thermodynamics and petrological applications. Contrib. Mineral. Petrol. 141,
998 659–686. doi:10.1007/s004100100267
999 Thy, P., Lesher, C.E., Fram, M.S., 1998. Low pressure experimental constraints on
1000 the evolution of basaltic lavas from Site 917, southeast Greenland continental
1001 margin, in: Saunders, A.D., Larsen, H.C., Wise, S.W., Jr. (Eds.), Proceedings

1002 of the Ocean Drilling Program, Scientific Results. pp. 359–372.
1003 doi:10.2973/odp.proc.sr.152.235.1998
1004 Toplis, M.J., 2005. The thermodynamics of iron and magnesium partitioning between
1005 olivine and liquid: criteria for assessing and predicting equilibrium in natural
1006 and experimental systems. Contrib. Mineral. Petrol. 149, 22–39.
1007 doi:10.1007/s00410-004-0629-4
1008 Tormey, D.R., Grove, T.L., Bryan, W.B., 1987. Experimental petrology of normal
1009 MORB near the Kane Fracture Zone: 22°–25° N, mid-Atlantic ridge. Contrib.
1010 Mineral. Petrol. 96, 121–139. doi:10.1007/BF00375227
1011 Villiger, S., Müntener, O., Ulmer, P., 2007. Crystallization pressures of mid-ocean
1012 ridge basalts derived from major element variations of glasses from
1013 equilibrium and fractional crystallization experiments. J. Geophys. Res. 112.
1014 doi:10.1029/2006JB004342
1015 Walker, D., Shibata, T., DeLong, S.E., 1979. Abyssal tholeiites from the
1016 Oceanographer fracture zone. Contrib. Mineral. Petrol. 70, 111–125.
1017 doi:10.1007/BF00374440
1018 Wanless, V.D., Shaw, A.M., 2012. Lower crustal crystallization and melt evolution at
1019 mid-ocean ridges. Nat. Geosci. 5, 651–655. doi:10.1038/ngeo1552
1020 Wilson, S.A., 1997. Data compilation for USGS reference material BHVO-2,
1021 Hawaiian Basalt (Open-File Report). US Geological Survey.
1022 Yang, H.J., Kinzler, R.J., Grove, T.L., 1996. Experiments and models of anhydrous,
1023 basaltic olivine-plagioclase-augite saturated melts from 0.001 to 10 kbar.
1024 Contrib. Mineral. Petrol. 124, 1–18. doi:10.1007/s004100050169
1025

1026

1027

Tables

Table 1: Compositions of synthetic starting compositions used in experiments in this study. Values in parentheses are 1.96 standard errors of the mean of replicate analyses in terms of least units cited, corresponding to the interval where 95% of the values are expected to lie.

Comment	N	SiO_2	TiO_2	Al_2O_3	FeO	MgO	CaO	Na_2O	Cr_2O_3	Total	CaO/Al_2O_3
C01a[a]	5	47.88(6)	0.88(2)	16.67(7)	9.41(9)	9.25(6)	12.77(10)	2.12(5)	0.0090(35)	99.00(18)	0.766(7)
CaAl01a[a]	6	47.98(6)	0.87(2)	16.85(7)	8.74(10)	9.33(2)	12.74(5)	2.25(4)	0.0111(26)	98.77(15)	0.756(4)
C02a[a]	7	47.69(17)	0.83(2)	16.43(5)	8.42(12)	9.31(5)	12.74(6)	2.15(3)	0.0014(88)	97.56(23)	0.776(4)
C02a[b]	7	48.88(12)	0.85(2)	16.84(6)	8.63(11)	9.54(5)	13.06(6)	2.21(3)	0.0014(90)	100.00	0.776(4)
C02a[c]	-	50.02	0.82	16.38	8.29	9.73	12.63	2.12	0	100.00	0.77
C01d[a]	5	48.59(16)	0.89(3)	16.72(6)	8.54(12)	8.97(5)	12.63(9)	2.17(4)	0.1745(76)	98.69(24)	0.755(6)
C02b[a]	13	47.99(11)	0.83(1)	16.40(5)	8.32(10)	9.04(3)	12.62(4)	2.20(2)	0.2247(101)	97.62(17)	0.769(4)
CaAl02[a]	12	47.81(6)	0.84(2)	15.76(6)	8.41(7)	9.29(3)	13.27(5)	2.13(4)	0.0053(62)	97.52(13)	0.842(4)
CaAl01c[a]	6	47.93(10)	0.88(1)	16.05(2)	8.66(11)	9.20(6)	13.62(6)	2.27(3)	0.0087(49)	98.62(18)	0.848(4)

[a] Analyzed with the electron microprobe at University of Freiburg. Data was normalized to USGS BHVO-2G contents of Jochum et al. (2005) based on averages of more than 50 analyses of this standard each week. [b] C02a[a], normalized to 100%. [c] Expected composition of C02a starting material, calculated from weighed masses of raw oxide materials used for mixing.

Table 2: Experimental conditions, phase proportions, Fe loss (calculated from mass balances using analyses of starting materials and phases in samples) as well as the calculated $^{Fe^{2+}-Mg}_{Ol\text{-}Liq}$. Bold numbers indicate samples where cpx was identified in the polished cross-section of the sample. For runs > #50, the oxygen fugacity which was calculated from Fe partitioning between platinum wires and liquid ('Calc') is used for further calculations instead of the value determined from oxygen sensor readings ('Sens') (see text for discussion).

Run	T / °C	t / h	log fO_2		Comp.	Phase proportion / wt%					Fe-loss / wt% (rel)	$^{Fe^{2+}-Mg}_{Ol\text{-}Liq}$
			Sens	Calc		gl	ol	fsp	cpx	sp		
#18	1175	24	-8.65		C01a	59.0	11.1	27.1	**2.8**	0.0	11.4(18)	0.288(4)
					C01d	51.7	7.8	28.2	**11.9**	0.4	3.0(22)	0.292(4)
#20	1190	24	-8.46	-7.28	C01a	70.5	9.5	19.9	0.0	0.0	4.3(12)	0.305(4)
					C01d	66.2	7.8	21.8	**3.9**	0.3	10.4(20)	0.309(4)
#22	1204	24	-8.18		C01a	81.5	6.4	12.1	0.0	0.0	3.8(11)	0.325(4)
					C01d	89.6	3.2	6.8	0.0	0.4	13.5(23)	0.347(6)
#24	1205	24	-8.35	-8.16	CaAl01a	78.8	6.5	14.7	0.0	0.0	12.4(13)	0.331(5)
					CaAl01c	90.5	2.8	6.7	0.0	0.0	5.1(15)	0.344(5)
#26	1175	24	-8.33	-5.43	CaAl01a	54.8	11.3	29.9	**4.0**	0.0	7.1(20)	0.264(4)
					CaAl01c	47.4	8.9	29.4	**14.4**	0.0	8.1(27)	0.272(7)
#29	1190	24	-8.39	-8.02	CaAl01a	60.6	9.5	25.2	4.7	0.0	16.8(18)	0.283(5)
					CaAl01c	79.3	6.7	14.2	**0.0**	0.0	0.6(18)	0.317(5)
#32	1186	48	-8.52		C01a	66.7	9.9	22.5	0.8	0.0	5.3(15)	0.299(5)
					C01d	67.3	8.7	22.1	**1.6**	0.3	7.9(22)	0.345(5)
#34	1186	96	-8.59	-8.96	C01a	66.4	10.1	23.5	0.0	0.0	21.9(14)	0.348(5)
					C01d	61.3	8.5	25.7	4.3	0.3	21.8(23)	0.369(7)
#36	1188	48	-7.99		CaAl01a	66.1	10.3	23.6	0.0	0.0	6.6(14)	0.338(6)
					CaAl01c	65.9	8.4	20.9	**4.8**	0.0	2.3(19)	0.301(5)
#37	1190	77	-8.67		CaAl01a	67.3	10.0	22.7	0.0	0.0	4.8(17)	0.323(4)
					CaAl01c	68.0	8.3	19.9	**3.7**	0.0	-1.6(16)	0.330(4)
#57	1205	24	-8.45	-3.87	C02a	73.7	7.3	19.0	0.0	0.0	-6.1(13)	0.182(2)
					C02b	66.6	3.9	22.1	**5.9**	1.5	1.6(30)	0.118(2)
					CaAl02	68.3	5.4	19.5	**6.8**	0.0	-1.8(25)	0.152(2)
#60	1217	24	-8.25	-3.45	C02a	77.1	6.0	16.9	0.0	0.0	4.0(17)	0.188(3)
					C02b	74.5	1.2	12.9	6.3	5.1	-11.1(90)	0.204(4)
					CaAl02	85.6	3.2	11.2	0.0	0.0	4.6(16)	0.189(3)
#63	1198	24	-8.42	-3.58	C02a	60.3	7.1	26.0	**6.6**	0.0	3.3(15)	0.118(2)
					C02b	56.4	4.8	26.6	**10.8**	1.5	7.1(29)	0.133(2)
					CaAl02	60.1	5.5	21.6	**12.8**	0.0	-0.4(15)	0.139(2)
#67	1205	48	-8.45	-5.29	C02a	70.9	8.1	21.0	0.0	0.0	2.3(16)	0.209(3)
					C02b	68.3	2.2	16.7	**9.3**	3.4	-5.9(62)	0.210(7)
					CaAl02	68.9	5.8	18.4	**6.9**	0.0	8.9(27)	0.210(4)
#78	1206	24	-8.45	-3.69	C02a	73.9	7.0	19.2	0.0	0.0	-6.0(15)	0.126(2)
					C02b	67.5	4.4	21.5	**5.1**	1.5	2.5(30)	0.102(2)
					CaAl02	69.9	5.1	19.2	**5.8**	0.0	-4.3(15)	0.124(2)

Table 3: Sources of data used to calibrate the equations for the crystallization model.

Source	System	P / GPa	T / °C	N
Presnall et al. (1978)	CMAS	0.0001	1266-1272	2
Walker et al. (1979)	Natural basalt	0.0001	1085-1235	11
Grove and Bryan (1983)	Natural basalt	0.0001	1137-1193	22
Onuma and Tohara (1983)	CMAS+Cr_2O_3	0.0001	1265	1
Baker and Eggler (1987)	Natural basalt	0.0001	1100-1122	4
		0.2	1020-1060	4
		0.8	1200-1250	4
Sack et al. (1987)	Natural basalt	0.0001	1064-1176	20
Tormey et al. (1987)	Natural basalt	0.0001	1152-1171	7
Juster et al. (1989)	Natural basalt	0.0001	1150-1180	4
Libourel et al. (1989)	CMAS	0.0001	1244-1275	24
Grove et al. (1990)	Natural basalt	0.0001	1108-1152	4
Shi and Libourel (1991)	CMAS+FeO	0.0001	1160-1220	27
Grove et al. (1992)	Natural basalt	0.0001	1161	1
		0.2	1126-1163	5
		0.8	1210-1265	10
		1	1235-1250	2
Shi (1993)	CMAS+FeO+Na_2O	0.0001	1100	16
Yang et al. (1996)	Natural basalt	0.0001	1100-1171	17
Reynolds and Langmuir (1997)	Natural basalt	0.0001	1175	3
Thy et al. (1998)	Natural basalt	0.0001	1111-1177	15
Libourel (1999)	CMAS+Na_2O+TiO_2+Cr_2O_3	0.0001	1229-1264	14
Sano et al. (2001)	Natural basalt	0.0001	1114-1175	17
Scoates et al. (2006)	Natural basalt	0.0001	1119	1
This study	Natural basalt	0.0001	1175-1206	15

Table 4: Coefficients of variables for description of $^{liq}_{Al}$, $^{liq}_{Ca}$, $^{liq}_{Mg}$ and T / °C in melts saturated in olivine, plagioclase and clinopyroxene. The equations are of the form $= + + {}^{liq}_{Na} + {}^{liq}_{K} + {}^{liq}_{Ti} + [...]$, where y is the variable in the first column and the values of a; b; … are the coefficients listed in the successive columns. The symbol $^{p}_{i}$ denotes the molar cation fraction of cation i in phase p. Rows labelled with ± are parameter errors (95% confidence level) of coefficients in the previous row.

Eq.	Const.	P / GPa	$^{liq}_{Na}$	$^{liq}_{K}$	$^{liq}_{Ti}$	$^{liq}_{Fe^{2+}}$	$^{liq}_{Fe^{3+}}$	$^{liq}_{Si}$	$(^{liq}_{Si})^2$	$^{liq}_{Si} \cdot {}^{liq}_{Ti}$	$^{liq}_{Cr}$	^{2}
$^{liq}_{Al}$	0.239	0.01801	0.162	0.485	-0.304	-0.320	-0.353	-0.130			5.652	1.192
±	0.004	0.00157	0.011	0.037	0.019	0.006	0.016	0.008			0.889	
$^{liq}_{Ca}$	1.070	-0.02707	-0.634	-0.618	-0.515	-0.188	-0.597	-3.044	2.477		-9.367	0.780
±	0.034	0.00242	0.016	0.052	0.032	0.009	0.026	0.142	0.146		1.424	
$^{liq}_{Mg}$	-0.173	0.00625	-0.541	-1.050	-0.182	-0.493	-0.028	1.599	-1.873		3.246	1.496
±	0.023	0.00162	0.011	0.039	0.019	0.005	0.016	0.099	0.105		0.973	
T / °C	679.1	46.8	-617.9	-699.1	3022	-627.6	-283.5	2689	-3056	-8228	-4799	4.948
±	39.5	3.5	14.8	45.5	224	7.4	26.1	166	173	525	1529	

Table 5: Coefficients of variables for description of the augite compositions in melts saturated in olivine, plagioclase and clinopyroxene. The equations give the molar fraction of the components $Mg_2Si_2O_6$ (enstatite), Fe_2Si_2O6 (ferrosilite), $Ca_2Si_2O_6$ (wollastonite), $NaAlSi_2O_6$ (jadeite), $NaCrSi_2O_6$ (ureyite), $CaAl_2SiO_6$ (Ca-Tschermak), $CaTiAl_2O_6$ (Ti-Tschermak) and $Ca(Fe^{3+})_2SiO_6$ (Fe-Tschermak). The equations are of the form $= + + {}^{liq}_{Na} + {}^{liq}_{K} + {}^{liq}_{Ti} + [...]$, where y is the variable in the first column and the values of a; b; … are the coefficients listed in the successive columns. The symbol ${}^{p}_{i}$ denotes the molar cation or component fraction of cation i in phase p. Rows labelled with ± are parameter errors (95% confidence level) of coefficients in the previous row.

Eq.	Const.	T / °C	P / GPa	$^{liq}_{Si}$	$^{liq}_{Ti}$	$^{liq}_{Al}$	$^{liq}_{Fe^{2+}}$	$^{liq}_{Fe^{3+}}$	$^{liq}_{Mg}$	$^{liq}_{Ca}$	$^{liq}_{Na}$	$^{liq}_{Cr}$	$(^{liq}_{Si})^2$	$(^{liq}_{Ti})^2$	$(^{liq}_{Na})^2$	^{2}
$^{cpx}_{Mg_2Si_2O_6}$	0.651	-0.00007	0.061	0.119	-0.415	-1.146	-0.566	0.330	1.686	-0.916	-0.297	-9.677				1.896
±	0.261	0.00010	0.011	0.219	0.309	0.372	0.222	0.455	0.190	0.217	0.177	7.550				
$^{cpx}_{Fe_2Si_2O_6}$	-0.024	-0.00008	0.055	0.647	0.134	-0.629	0.701	0.720	-0.564	-0.081	0.008	-7.279				1.384
±	0.243	0.00008	0.008	0.211	0.332	0.381	0.217	0.427	0.166	0.214	0.157	5.069				
$^{cpx}_{Ca_2Si_2O_6}$	1.916	0.00021	-0.130	-1.954	-2.078	-2.517	-1.251	-4.669	-0.805	-1.480	-0.643	-17.631				0.561
±	0.464	0.00018	0.019	0.395	0.526	0.645	0.398	0.728	0.355	0.390	0.329	12.074				
$^{cpx}_{NaAlSi_2O_6}$	-0.244	-0.00005	0.021	0.109	0.764	0.506	0.333	0.735	0.044	0.278	0.320	-25.445	0.114	-4.693	0.451	0.234
±	0.239	0.00009	0.010	0.686	0.365	0.305	0.203	0.212	0.238	0.287	0.300	5.925	0.654	5.500	1.723	
$^{cpx}_{NaCrSi_2O_6}$	-0.490	0.00017	-0.039	0.320	0.457	0.489	0.229	0.099	0.181	0.066	0.299	36.836				0.345
±	0.407	0.00018	0.015	0.340	0.695	0.561	0.315	0.377	0.313	0.424	0.351	6.618				
$^{cpx}_{CaAl_2SiO_6}$	-1.821	0.00026	0.028	1.358	1.515	3.206	1.156	2.852	-0.499	2.347	0.746	35.276				0.398
±	0.417	0.00016	0.016	0.348	0.474	0.641	0.365	0.458	0.303	0.349	0.275	11.761				
$^{cpx}_{CaTiAl_2O_6}$	0.331	0.00002	-0.002	-0.471	-0.208	-0.165	-0.070	0.011	-0.665	-0.124	-0.102	6.015				1.174
±	0.128	0.00004	0.005	0.114	0.129	0.209	0.136	0.154	0.138	0.160	0.122	3.026				
$^{cpx}_{CaFe^{3+}_2SiO_6}$	-0.004	-0.00005	-0.004	0.154	0.329	-0.261	-0.816	0.790	0.020	0.682	0.426	-15.453				0.010
±	3.490	0.00130	0.518	3.338	11.007	4.247	2.812	3.190	3.939	4.806	3.903	105.915				

Figures

Fig. 1 Plots of MgO contents vs. concentrations of other oxides in glass samples from 24 h duration experiments run at QFM with different starting composition. Concentrations are weight percent, and FeO is total iron.

Fig. 2 Plots of MgO contents vs. concentrations of other oxides in glass samples from 24 h duration oxidized experiments with different starting composition. Concentrations are weight percent, and FeO is total iron.

Fig. 3 Plot of log fO_2 measured by the oxygen sensor versus (a) log fO_2 calculated from Fe concentrations of Pt wires used in the experiments, and (b) log fO_2 calculated using the model of Toplis (2005) for the olivine-liquid Mg-Fe exchange equilibria.

Fig. 4 Plots of phase assemblages for (a) QFM experiments and (b) oxidized experiments, determined by electron microprobe, distinguishing samples above and below clinopyroxene saturation. For both experimental sets, a systematically earlier saturation with cpx can be observed for Cr-spinel saturated and high Ca/Al experiments. Furthermore, higher absolute temperatures of cpx crystallization are evident for oxidized experiments in comparison to samples produced at QFM conditions.

Fig. 5 Plot of crystallization pressures estimated by cpx geobarometers of Herzberg (2004); Villiger et al. (2007); Yang et al. (1996) as well as by the new geobarometer

calibration developed in this study, for experimental samples of this study. The upper part (a) shows experiments run at QFM, while the lower part (b) shows runs at oxidizing conditions.

Fig. 6 Olivine/plagioclase ratios (modes) in the crystallizing assemblage predicted by calculation of the OPAM location using equations in Table 4 versus the same ratio calculated from the actual melt composition for experiments of this study saturated in olivine and plagioclase. Both ratios result from the projection of the melt to the cpx-ol-plag pseudoternary.

Fig. 7 Comparison of predictions of liquid evolution during fractional crystallization for starting composition C01a using models from this study, Yang et al. (1996), Ariskin et al. (1993), Langmuir et al. (1992) and MELTS (Asimow and Ghiorso, 1998; Ghiorso and Sack, 1995) with glass compositions of experimental samples of 24 h runs. Oxygen fugacity is constrained to conditions of the QFM buffer in all model runs. In addition, the model from this study was run using a bulk composition assuming 10 wt% iron loss, similar to the largest amount indicated by mass balances for experimental samples. All concentrations are in weight percent.

Fig. 8 Comparison of liquid evolution paths predicted by the model in this study with fO_2 constrained to the QFM buffer. The solid thin line shows the prediction for composition C01d with 0.38 wt% Cr-spinel removed in order to achieve chromium contents similar to experimental values (i.e. using a starting composition containing 0.07 wt% Cr_2O_3), and dashed lines show predictions by the crystallization model using bulk compositions with higher chromium contents of 0.14 and 0.21 wt% Cr_2O_3.

The model prediction with the same composition, except for chromium, which was set to zero, is shown by the dotted line.

Fig. 9 Histograms showing the distribution of crystallization pressures calculated from equations in Table 4 and equations of Villiger et al. (2007) and Herzberg (2004) for glass analyses from the East Pacific Rise (EPR), Mid Atlantic Ridge (MAR) and South-West Indian Ridge (SWIR) obtained from the PetDB database (Lehnert et al., 2000). For comparison, pressures were also calculated using equations in Table 4 but without Cr. Primitive glasses with $Mg\#_{liq} > 0.6$, analyses without chromium measurements, as well as data of enchriched MORB (based on $K_2O/TiO_2>0.2$) was excluded from the data sets (see text for details). The dashed lines and the numbers at the top at each diagram shows the trimmed means $\bar{}$ (ignoring the 5% lowest and highest pressures) of the pressure distributions, which are not located at the most frequent pressure for most histograms because the distributions are slightly skewed. N is the total number of samples.

Fig. 10 Histograms showing the distribution of crystallization pressures calculated from equations in Table 4 and equations of Villiger et al. (2007) and Herzberg (2004) for glass analyses of Jenner and O'Neill (2012). The data set was divided into intermediate- to fast-spreading ridges and slow-spreading ridges with full spreading-rates less than 55 mm/year. For comparison, pressures were also calculated using equations in Table 4 but without Cr. See caption of Figure 9 and text for details.

Fig. 11 Plot of pressures estimated for a typical MORB composition (see text for details) as function of chromium content, predicted by the $^{liq}_{Ca}$ equation in Table 4 (black lines). The red circles show the location of the original chromium content.

Supplementary material

Supplementary Table 1 Electron microprobe analyses of phases in experimental samples. All concentrations are given in weight percent, and FeO is total iron. N is the number or replicate analyses. Phase abbreviations are: Glass gl; Olivine ol; plagioclase plag; Clinopyroxene cpx; Spinel sp. σ(x) values are 1.96 standard errors of replicate analyses.

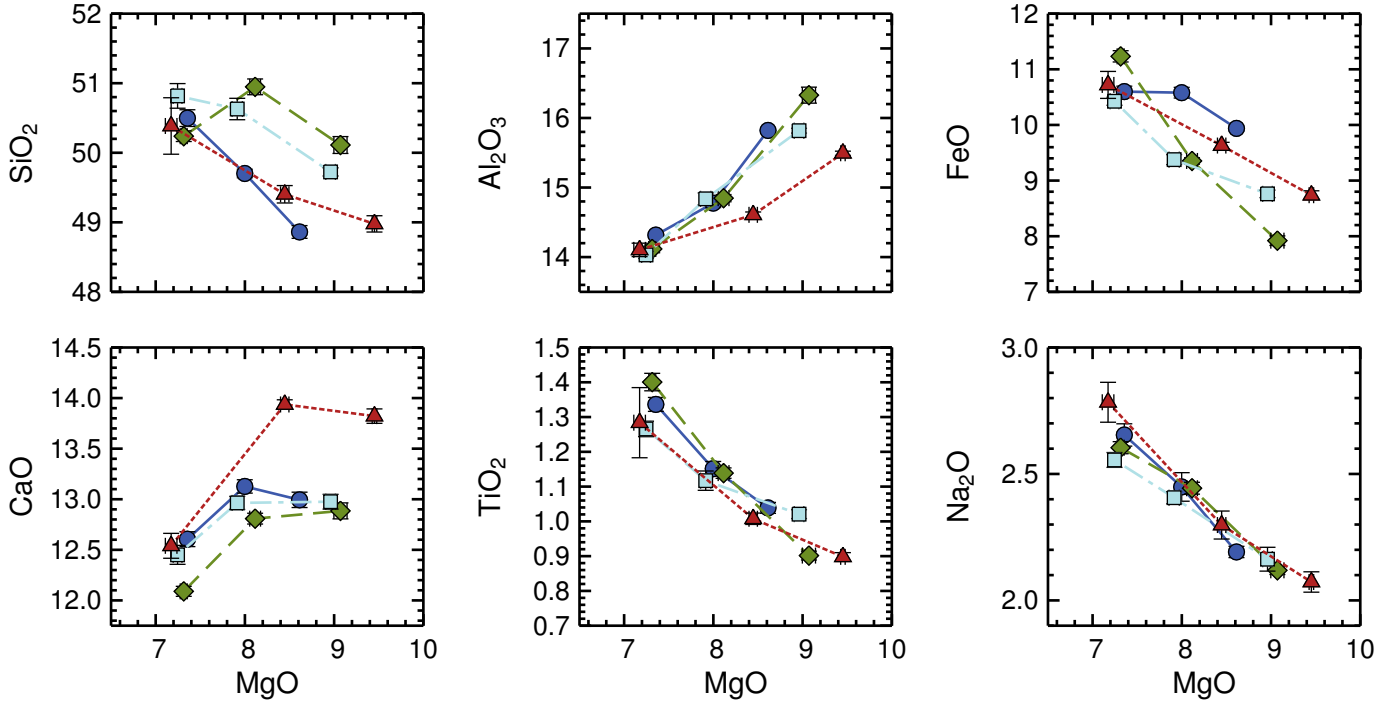
SiO2
Al2O3
FeO
CaO
TiO2
Na2O
MgO
MgO
MgO
C01a (Cr-free, normal Ca/Al)
C01d (chromite-saturated)
CaAl01a (Cr-free, normal Ca/Al)
CaAl01c (higher Ca/Al)

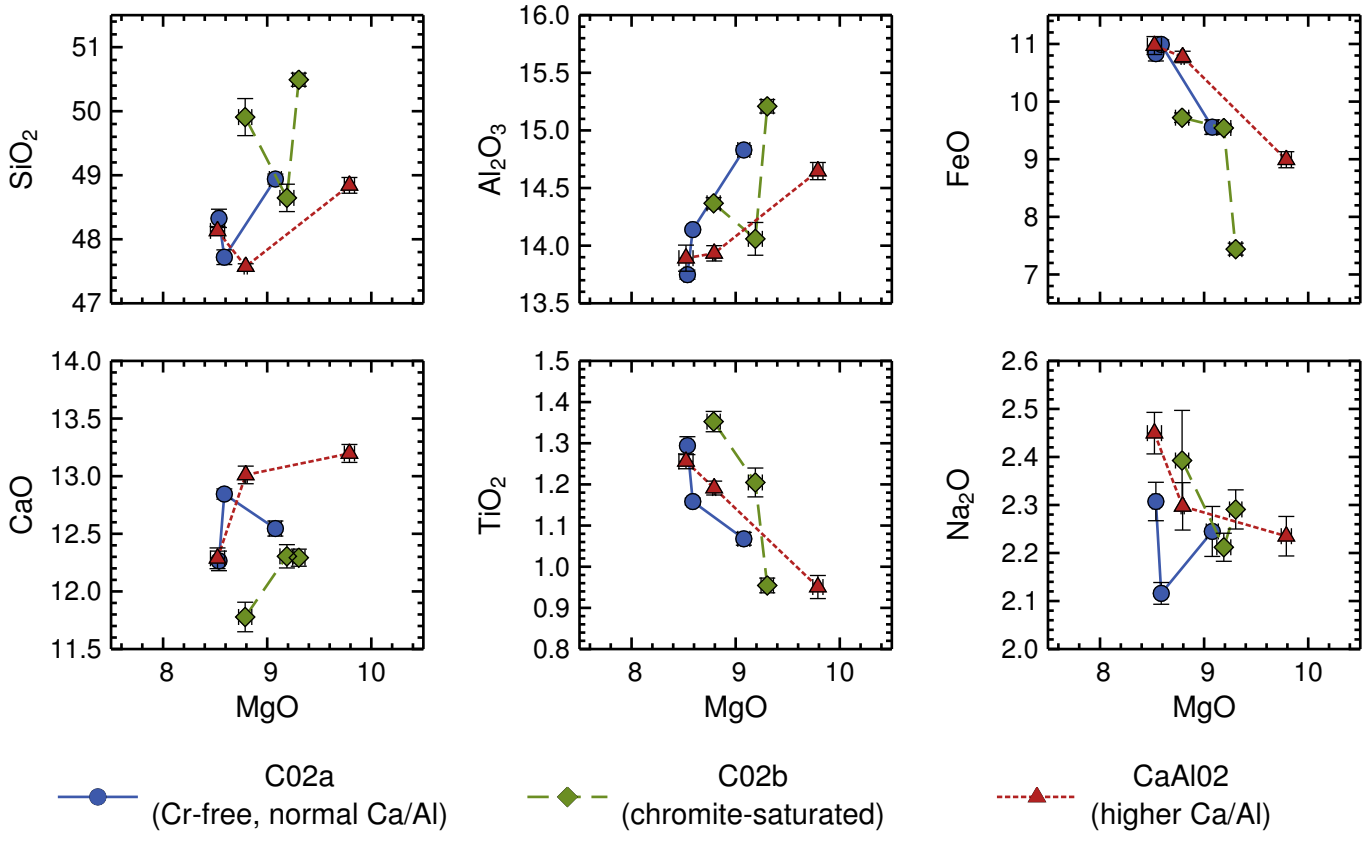
SiO2
Al2O3
FeO
CaO
TiO2
Na2O
MgO
C02a
(Cr-free, normal Ca/Al)
C02b
(chromite-saturated)
CaAl02
(higher Ca/Al)

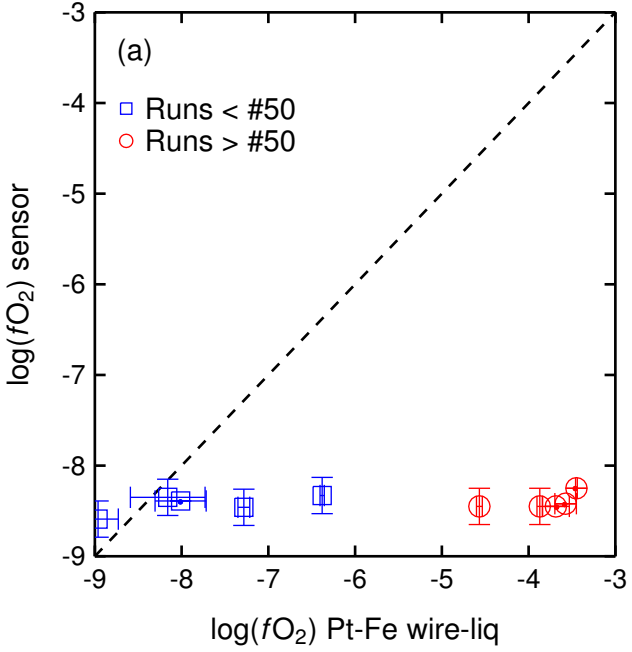
(a)
Runs < #50
Runs > #50
log(fO_2) sensor
log(fO_2) Pt-Fe wire-liq
-3
-4
-5
-6
-7
-8
-9

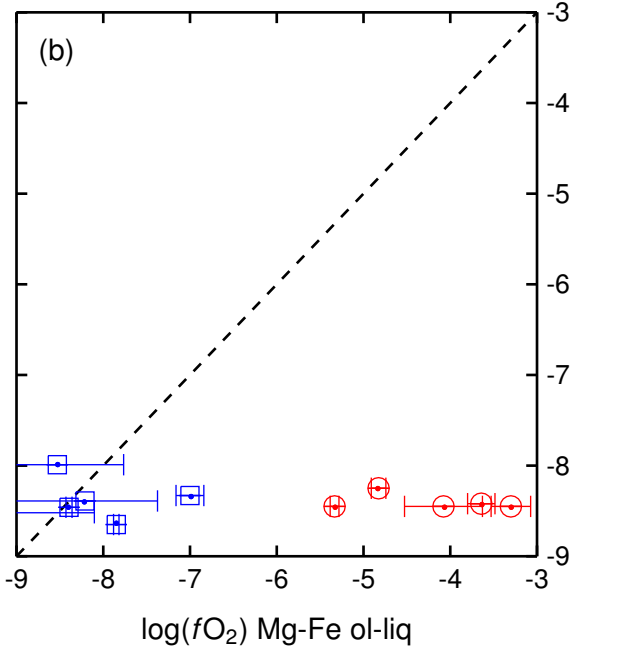
(b)
log(fO_2) Mg-Fe ol-liq
-3
-4
-5
-6
-7
-8
-9

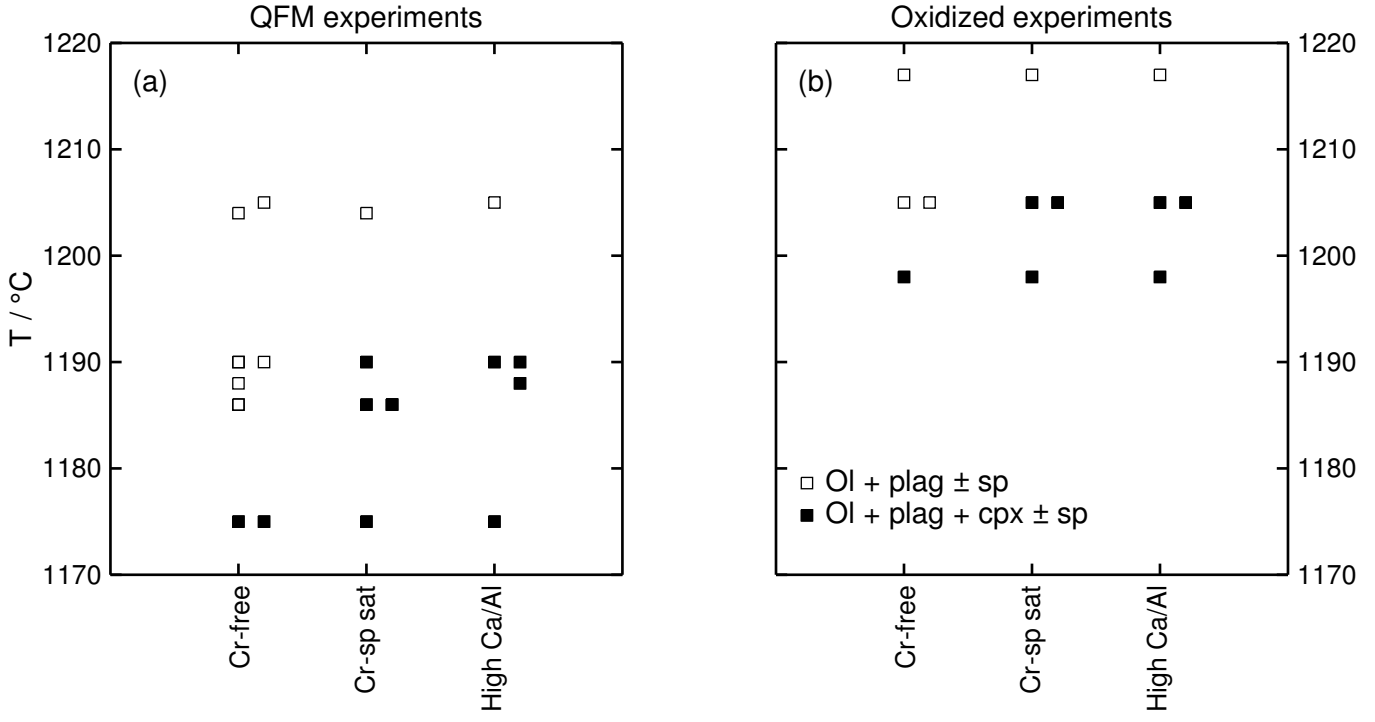
QFM experiments
(a)
T / °C
1220
1210
1200
1190
1180
1170
Cr-free
Cr-sp sat
High Ca/Al
Oxidized experiments
(b)
Ol + plag ± sp
Ol + plag + cpx ± sp
1220
1210
1200
1190
1180
1170
Cr-free
Cr-sp sat
High Ca/Al

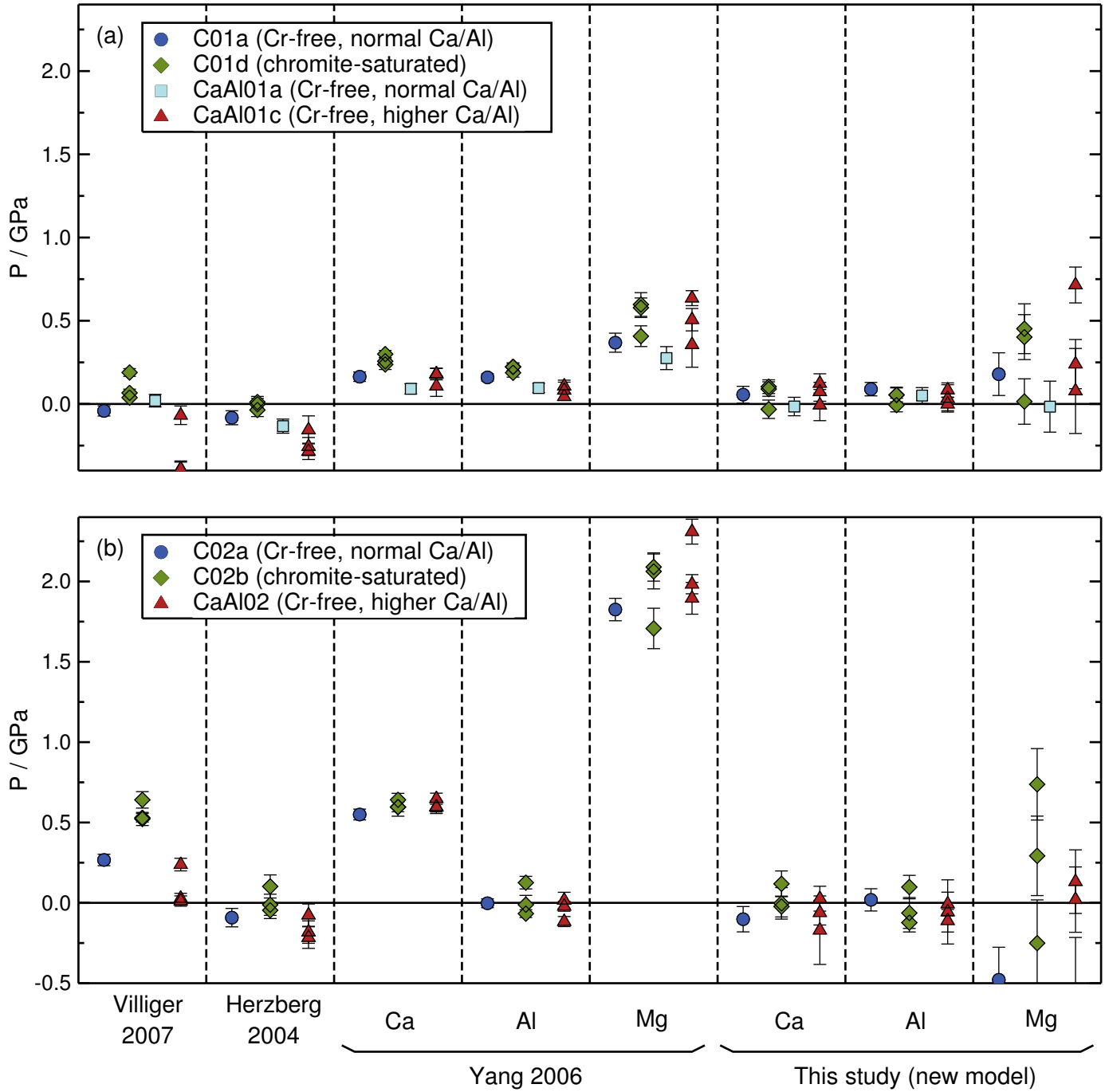
(a)
C01a (Cr-free, normal Ca/Al)
C01d (chromite-saturated)
CaAl01a (Cr-free, normal Ca/Al)
CaAl01c (Cr-free, higher Ca/Al)
P / GPa
2.0
1.5
1.0
0.5
0.0
(b)
C02a (Cr-free, normal Ca/Al)
C02b (chromite-saturated)
CaAl02 (Cr-free, higher Ca/Al)
P / GPa
2.0
1.5
1.0
0.5
0.0
-0.5
Villiger 2007
Herzberg 2004
Ca
Al
Mg
Ca
Al
Mg
Yang 2006
This study (new model)

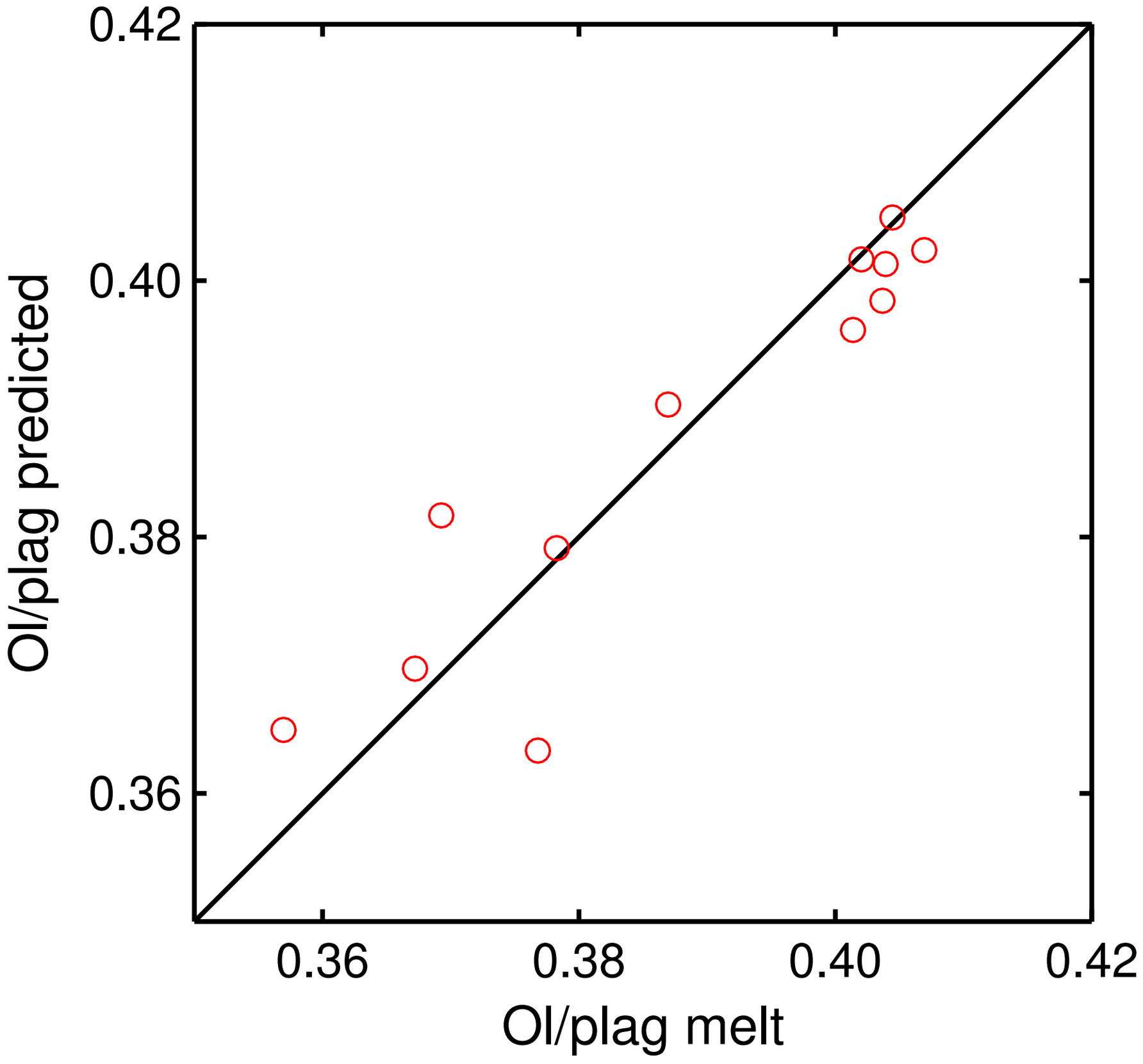
0.42
0.40
0.38
0.36
Ol/plag predicted
0.36
0.38
0.40
0.42
Ol/plag melt

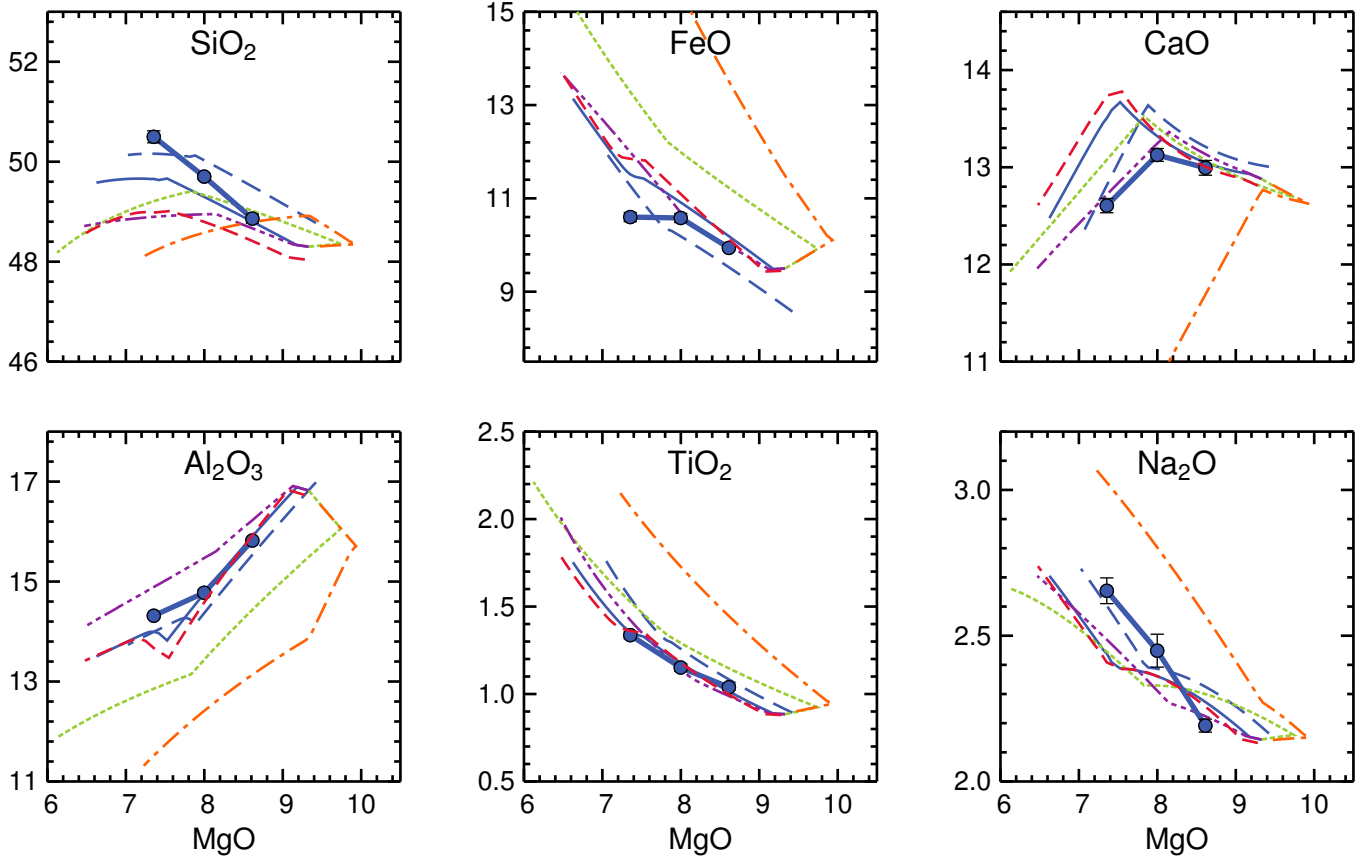
SiO2
FeO
CaO
Al2O3
TiO2
Na2O
MgO
MgO
MgO
Exp. data
Yang 1996
MELTS
This study
Ariskin 1993
Langmuir 1992
This study (with Fe loss)

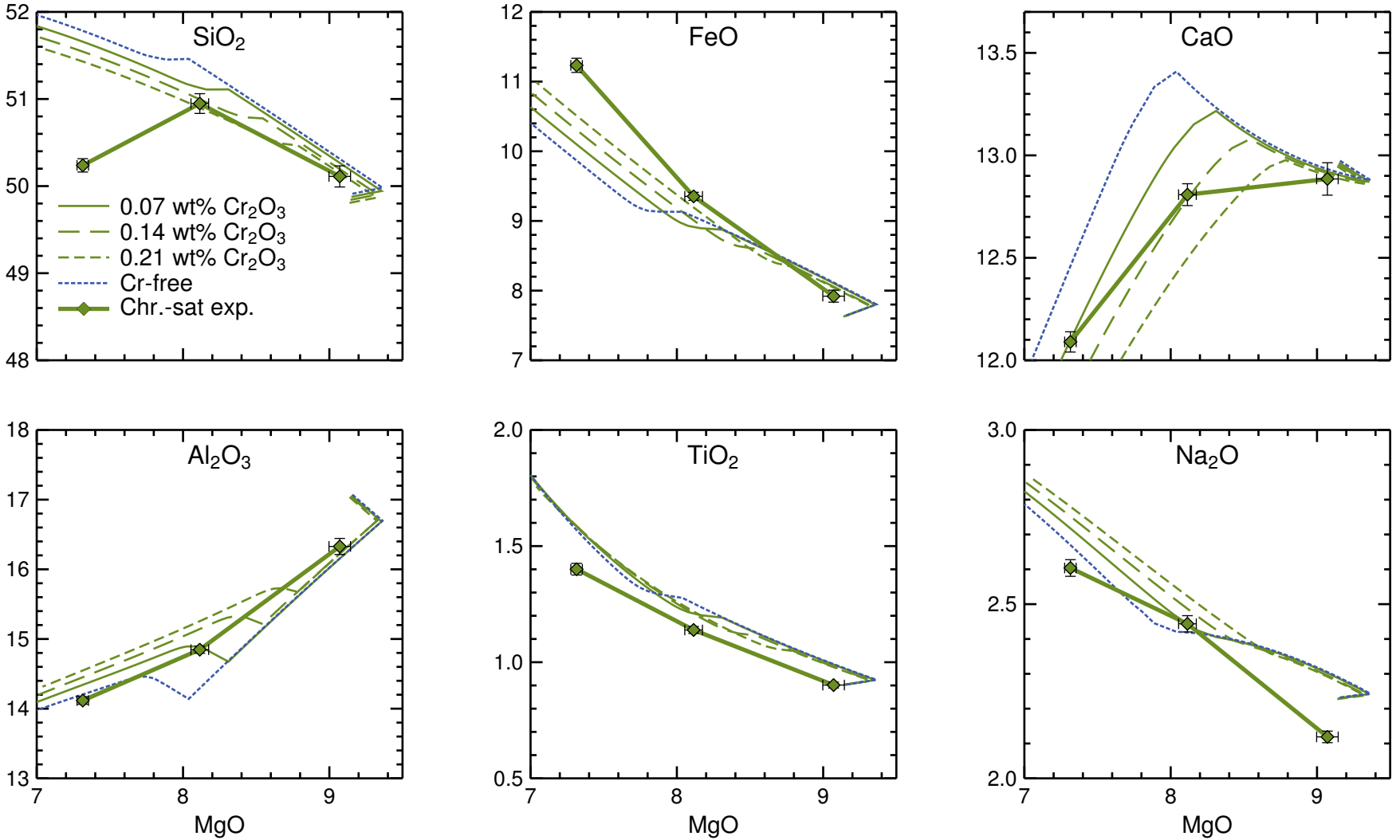
SiO2
FeO
CaO
Al2O3
TiO2
Na2O
0.07 wt% Cr2O3
0.14 wt% Cr2O3
0.21 wt% Cr2O3
Cr-free
Chr.-sat exp.
MgO
MgO
MgO

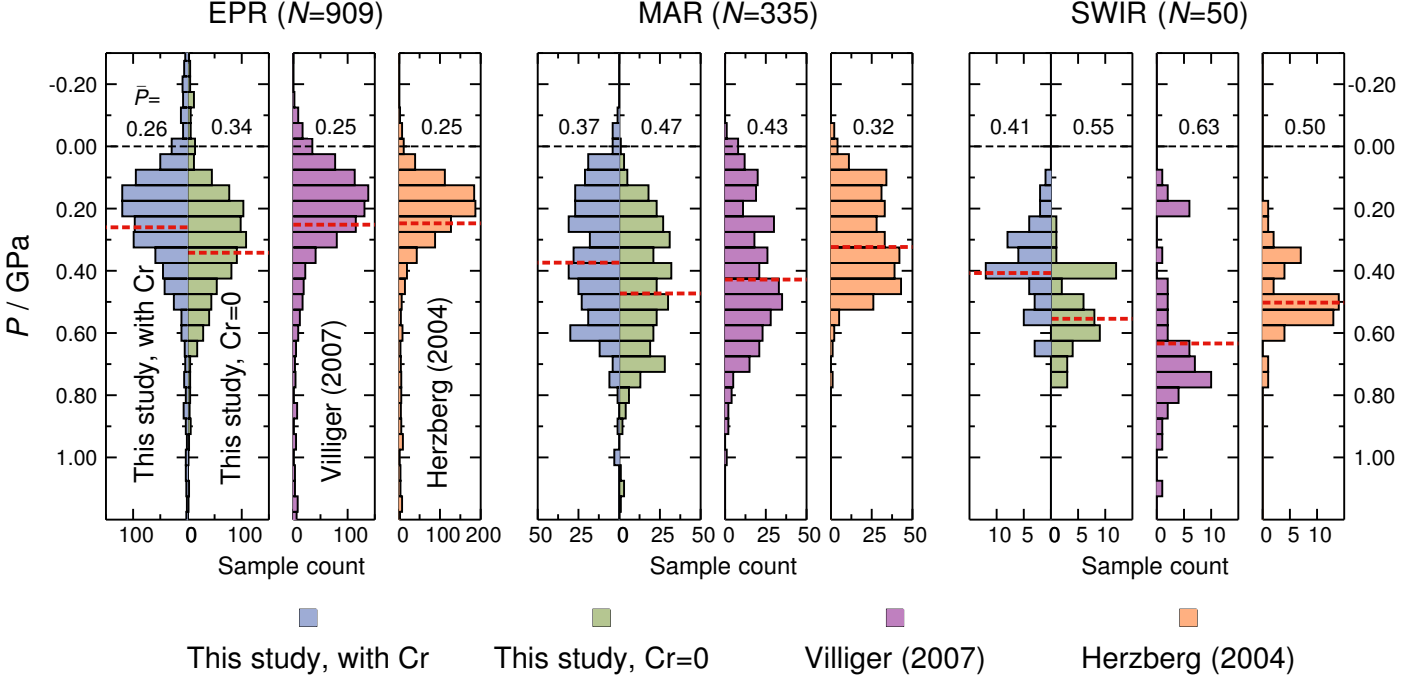
EPR (N=909)
MAR (N=335)
SWIR (N=50)
P / GPa
$\bar{P}$=
0.26
0.34
0.25
0.25
0.37
0.47
0.43
0.32
0.41
0.55
0.63
0.50
This study, with Cr
This study, Cr=0
Villiger (2007)
Herzberg (2004)
Sample count
This study, with Cr
This study, Cr=0
Villiger (2007)
Herzberg (2004)

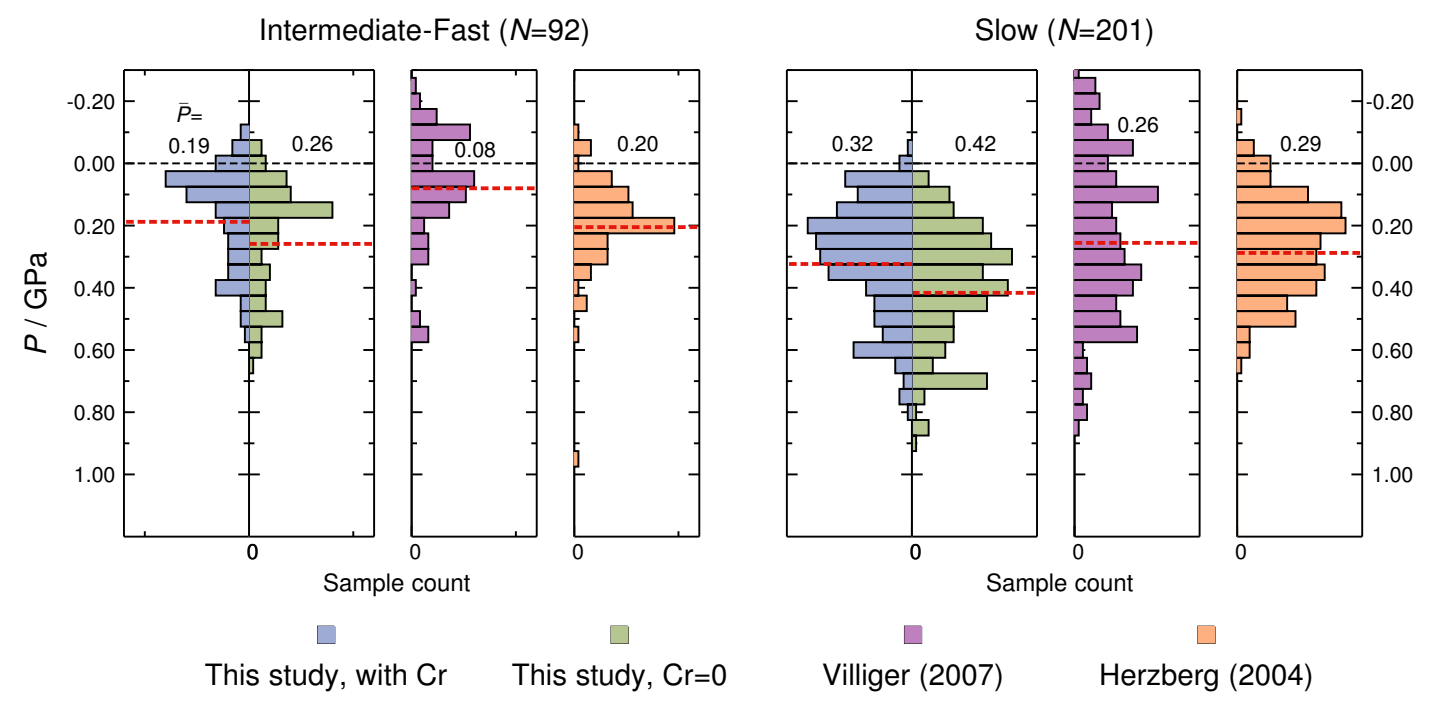
Intermediate-Fast (N=92)
Slow (N=201)
P / GPa
-0.20
0.00
0.20
0.40
0.60
0.80
1.00
P̄=
0.19
0.26
0.08
0.20
0.32
0.42
0.26
0.29
0
Sample count
This study, with Cr
This study, Cr=0
Villiger (2007)
Herzberg (2004)

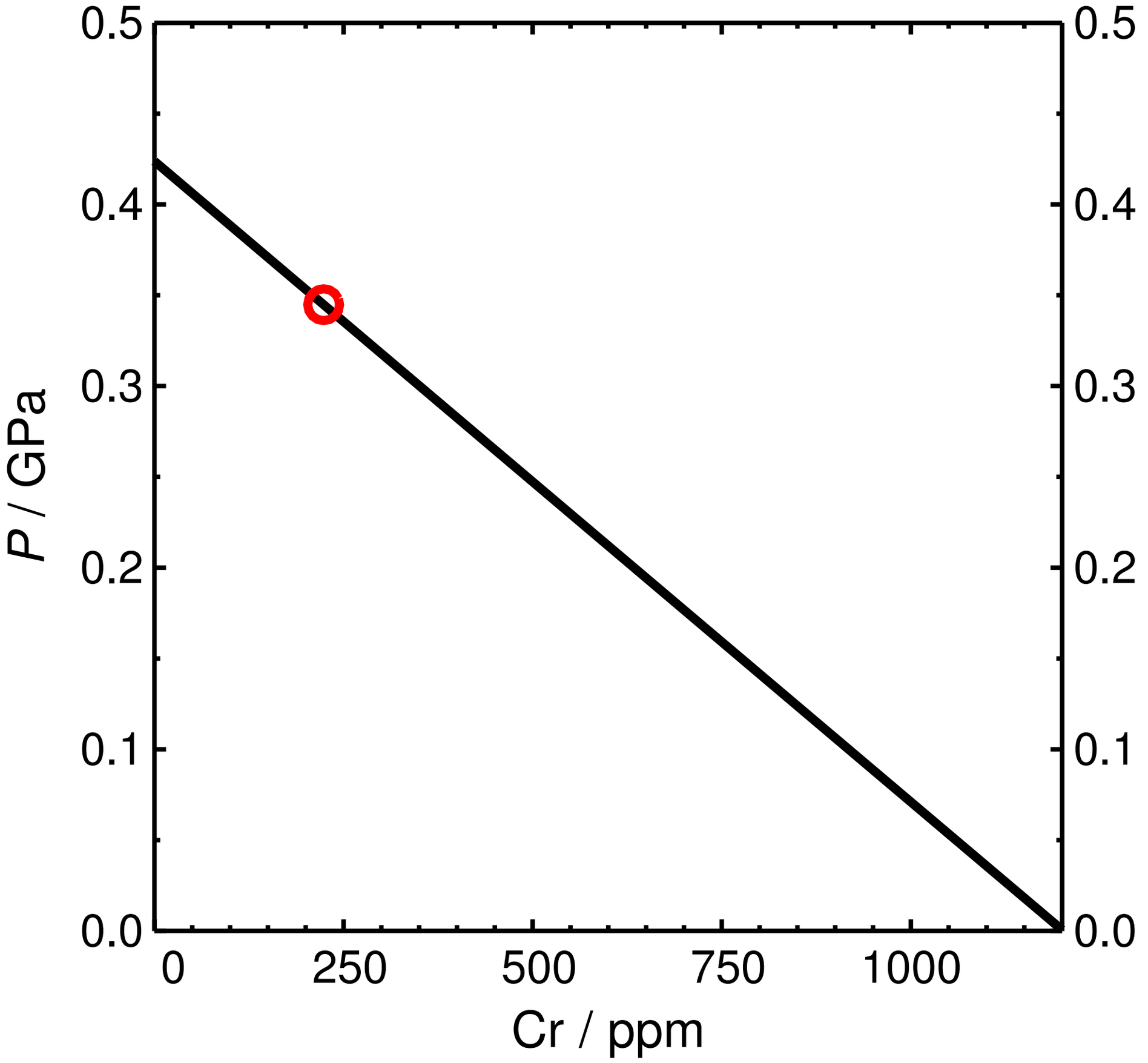
0.5
0.4
0.3
0.2
0.1
0.0
P / GPa
0
250
500
750
1000
Cr / ppm